Pore solution composition of alkali-activated slag/fly ash pastes

Zuo, Yibing; Nedeljkovic, Marija; Ye, Guang

DOI
10.1016/j.cemconres.2018.10.010

Publication date
2019

Document Version
Accepted author manuscript

Published in
Cement and Concrete Research

Cement and Concrete Research, 115(2019) 230-250

Pore solution composition of alkali-activated slag/fly ash pastes

Yibing Zuo, Marija Nedeljković, Guang Ye

Section of Materials and Environment, Faculty of Civil Engineering and Geosciences, Delft University of Technology, Stevinweg 1, 2628 CN Delft, The Netherlands

Abstract: The pore solutions of a series of hardened alkali-activated slag/fly ash pastes were extracted by the steel-die method, and analyzed using ICP-OES analysis technique. According to the saturation index from thermodynamic calculations, the pore solutions of alkali-activated slag pastes kept oversaturated with respect to solid reaction products with time. In the pore solutions of alkali-activated fly ash pastes, an increase of temperature (from 40 °C to 60 °C) led to decreases of the concentrations of Si, Al, Ca, Na, OH^-, K, Fe and Mg, while the soluble silicate in the alkaline activator resulted in increases of the concentrations of these elements. Compared to the alkali-activated slag paste with the same alkaline activator, 50% replacement of slag by fly ash did not result in a substantial change of the pore solution composition. Based on the experimental results, conceptual models were proposed to describe the elemental concentrations in the pore solutions.

Keywords: alkali activation; slag/fly ash; pore solution; saturation index; conceptual models

1 Introduction

Alkali-activated materials (AAMs) are a class of materials obtained by the chemical reaction of a powdered aluminosilicate precursor (most commonly blast furnace slag and/or fly ash) with an alkaline activator (usually a solution of sodium hydroxide and/or sodium silicate) at ambient or elevated temperature [1, 2]. Due to the ability to utilize high-volume of industrial by-products as the powdered aluminosilicate precursors, AAMs can save a large amount of fossil fuel-derived energy. As such, 80% or greater reduction of CO_2 emission can be achieved by AAMs when compared to ordinary Portland cement (OPC) based materials [3, 4]. Besides, AAMs release lower amount of heat [5], and provide comparable or even superior mechanical properties and durability performance [3, 6-9]. Therefore, AAMs show very promising potential for utilization to embrace a sustainable future global construction materials industry [2].

Pore solution is an essential component of AAMs. It is in this medium where the powdered aluminosilicate precursors dissolve and subsequently a set of reactions take place to produce solid reaction products. The role of pore solution can be viewed in the following three aspects.

- *Dissolution kinetics*. The high concentration of OH^- ions in the pore solution allow breaking of bonds such as Si-O and Al-O on the surface of aluminosilicate precursors [10]. A higher alkalinity of pore solution will accelerate the dissolution kinetics [11-15]. Therefore, from the kinetics point of view, pore solution composition determines the dissolution kinetics of aluminosilicate precursors. The dissolution kinetics determines the degree of reaction and thus controls the reaction kinetics and the amount of solid reaction products produced with time.

- *Thermodynamics*. Thermodynamics is of great significance to the understanding of chemical reactions [16]. The reactions of AAMs, same as any other chemical system, follow the law of thermodynamics. When aluminosilicate precursors are brought into contact with an alkaline activator, their constituents start to dissolve and subsequently various solid reaction products start to be formed if the solution is saturated or oversaturated with respective the solids. At the given temperature and pressure, the pore solution composition controls the ongoing reaction process and determines what reaction products are to be formed [17, 18].

- *Durability*. The dominant phase assemblage in AAMs is an alkali calcium-aluminosilicate hydrate (C-(N-)A-S-H) type gel or a three-dimensional hydrous alkali-aluminosilicate (N-A-S-H) type gel, depending on the Ca content in the system [1]. From the durability point of view, the high alkalinity of pore solution ensures the stability of calcium-aluminosilicate hydrates [19] and alkali-aluminosilicate gels [20] in AAMs. If AAMs are embedded with reinforcing steel, the pore solution plays a more important role by forming a passive film on the surface of steel rebars and, consequently, avoiding corrosion of steel rebar [21, 22].

Those three aspects illustrate the significance of pore solution in AAMs. Furthermore, the chemical properties (chemical composition, and amorphous content etc.) and physical properties (surface morphology, and particle size etc.) of aluminosilicate precursors vary significantly from different sources [1, 5, 23]. For this reason, the alkali activation of aluminosilicate precursors greatly relies on the pore solution. However, studies regarding the pore solution composition in

AAMs are few for alkali-activated slag paste [12, 24-26], and even rarely reported for alkali-activated fly ash paste and alkali-activated slag blended with fly ash paste.

Song and Jennings studied the pore solution chemistry of alkali-activated slag and found that higher alkalinity of pore solution led to higher concentrations of Si and Al and lower concentrations of Ca and Mg [24]. In another study regarding the relationship between the composition of pore solution and the composition and structure of the main reaction products in alkali-activated slag paste, the researchers found that the nature of the alkaline activator influenced the structure and composition of the produced calcium silicate hydrate [25]. In comparison with the pore solution of OPC-based materials, the pore solution of alkali-activated slag paste showed ten times lower concentration of Ca and tens to hundreds of times higher concentrations of Si and Na [12]. It was reported that the initiation of pitting at the steel-cement concrete interface started only after the concentration ratio of Cl^- relative to OH^- exceeded a particular value [22]. This suggests a great dependence of passivation of reinforcing steel on the alkalinity of the pore solution. Because of little soluble Ca available in the pore solution of alkali-activated slag to play a buffering role similar to $Ca(OH)_2$ in OPC-based materials, the alkalinity of pore solution of alkali-activated slag is mainly maintained by the content of alkali [26]. Therefore, it is essential to provide sufficient amount of alkalis to ensure protection of reinforcing steel from corrosion.

In this study, the pore solutions of alkali-activated slag, alkali-activated fly ash and alkali-activated slag blended with fly ash pastes were studied by means of the inductively coupled plasma-optical emission spectroscopy (ICP-OES) analysis technique. The influences of alkaline activator and temperature on the pore solution composition were investigated. The measured

composition of the pore solution and its changes with time can be used to predict the (potentially) solid reaction products. Thus, the pore solutions of alkali-activated slag pastes were thermodynamically analyzed in terms of effective saturation index. In the meantime, solid phase analysis was conducted through the X-ray diffraction (XRD) and Fourier transform infrared spectroscopy (FTIR). Based on the experimental results, conceptual models were proposed to describe the elemental concentrations in the pore solutions. The obtained results will contribute to new insights regarding the chemistry of pore solution and thermodynamic modelling in AAMs.

2 Materials and methods

2.1 Materials and mixtures

In this study, ground granulated blast furnace slag and fly ash were used as the aluminosilicate precursors to prepare alkali-activated slag/fly ash pastes. The chemical compositions of blast furnace slag and fly ash were determined by X-ray fluorescence spectrometry (XRF), and are listed in Table 1. The X-ray diffraction patterns of slag and fly ash are plotted in Figure 1. Quartz, mullite and hematite were the three crystalline phases identified in fly ash. In order to determine the amorphous content of fly ash, corundum (α-Al_2O_3) was added as an internal standard to replace 20% of fly ash. Through the Rietveld analysis method [27], the amorphous content of fly ash was determined as 71%. By subtracting SiO_2 and Al_2O_3 in the crystalline phases from the total SiO_2 and Al_2O_3, the reactive SiO_2 and Al_2O_3 were determined as 37% and 15% respectively. These results agree with the measurements by a previous colleague using the chemical dissolution treatment (we used a similar fly ash from the same manufacture plant in Netherlands) [28]. For slag, no crystalline phase was identified from the X-ray diffraction pattern. This is

consistent with the fact that the ground granulated blast furnace slag usually contains more than 95% vitreous phase [29].

Table 1 Chemical compositions of blast furnace slag and fly ash (by weight, %)

Figure 1 X-ray diffraction patterns of slag and fly ash. In the graph, Q, M and H refer to quartz, mullite and hematite respectively.

Sodium hydroxide (analytical grade, >98%) and water glass (8.25 wt.% Na_2O, 27.5 wt.% SiO_2 and 64.25 wt.% H_2O) were used to prepare two types of alkaline activators: sodium hydroxide activator and sodium silicate activator. As shown in Table 2, a series of alkaline activators with different contents of NaO_2 and SiO_2 were used to prepare alkali-activated slag pastes, alkali-activated fly ash pastes and alkali-activated slag blended with fly ash pastes. In the notations for the samples, N and S indicate weight percentage of Na_2O and SiO_2 with respect to the precursor, T indicates temperature in Celsius and B indicates blend of slag and fly ash. The Na_2O in alkaline activator consists of the Na_2O from sodium hydroxide and the Na_2O from water glass. For alkali-activated slag pastes and alkali-activated slag blended with fly ash pastes, water to precursor ratio was 0.4. For alkali-activated fly ash pastes, water to precursor ratio was 0.35. Here, the water in water glass was also included in the calculation of the water to precursor ratio of the pastes. According to the type of alkaline activator, the samples were categorized into two systems: sodium hydroxide activated system (with no soluble silicate in the alkaline activator) and sodium silicate activated system (with soluble silicate in the alkaline activator).

Table 2 Mixture compositions and curing temperature

According to the materials characterization described previously, fly ash contains glassy (amorphous) and crystalline constituents in nature, e.g. quartz, mullite and hematite. Compared to slag, fly ash has much lower reactivity. Therefore, elevated temperature curing is usually applied for the alkali activation of fly ash in order to obtain a relatively high strength at early ages [28, 30]. The elevated temperature leads to an acceleration of the dissolution of fly ash and the polymerization process of alkali-aluminosilicate type gel [1, 31]. In this study, two elevated temperatures (40 °C and 60 °C) were used to investigate the influence of temperature on the pore solution composition. For all samples, sealed curing was applied until testing.

The pH and concentrations of Na, Si, and OH^- in the alkaline activators are listed in Table 3. These results were obtained through the thermodynamic calculations using a thermodynamic software. This software is introduced in the section 2.3. In sodium hydroxide solution, aqueous sodium hydroxide (NaOH(aq)) normally exists. For this reason, the measured concentration of OH^- through titration against hydrochloride acid includes the hydroxide from NaOH(aq). The details of titration against hydroxide acid are given in section 2.2. As derived by thermodynamic calculations, two values of the concentration of OH^-, e.g. including and excluding hydroxide from NaOH(aq), are provided in Table 3. A big difference can be seen between those two values for each alkaline activator, and the concentration of OH^- including hydroxide from NaOH(aq) is closer to that in the pore solution of alkali-activated slag/fly ash pastes, as obtained by titration.

Table 3 The pH and concentrations of Na, Si, and OH^- in the alkaline activators

2.2 Pore solution analysis via ICP-OES

The pore solutions of hardened samples were extracted using the steel-die method as described by Barneyback and Diamond [32]. Pressures of up to 300 MPa were used to extract the pore fluid from the samples at different curing ages. After extraction, the pore solution was immediately filtered using Whatman 41 filter paper. One part of the filtered solution was diluted using nitric acid (0.2 vol.%). The diluted solutions were analyzed through a PerkinElmer Optima 5300DV ICP-OES spectrometer, by which the concentrations of Si, Al, Ca, Na, K, Fe and Mg were determined.

The concentration of OH^- was measured by titration against hydrochloride acid (0.1 mol/L). Phenolphthalein was used as the indicator. First, a volume (V_1, ml) of pore solution was accurately measured using a pipette and injected into a beaker. Then a drop of phenolphthalein was added into the beaker, and the solution turned red. Afterwards, hydrochloride acid was slowly added into the beaker through a burette until the solution turned colorless. While adding hydrochloride acid, the beaker was swirled with hand. After the titration, the amount of hydrochloride acid added into the beaker was measured as V_2 (ml). Then the concentration of OH^- ($[OH^-]$, mol/L) could be determined as:

$$[OH^-] = 0.1*V_2/V_1 \quad (1)$$

In the titration test, two replicates of each pore solution were titrated, and the average $[OH^-]$ was presented as the final result.

For the measurement of S, another part of the filtered solution was diluted using sodium hydroxide solution (0.1 mol/L) instead of nitric acid, and subsequently subject to ICP-OES

194 analysis. This is because S mostly exists as sulfide (HS^-) in the pore solution [12, 33]. The
195 dilution with nitric acid will acidify HS^- and lead to formation of H_2S as described by Equation
196 (2). On one hand, H_2S evaporates and results in a characteristic foul odor of rotten eggs, as
197 experienced during the dilution process using nitric acid. On the other hand, H_2S may be oxidized
198 and lead to white precipitation of sulfur as described by Equation (3), and shown in Figure 2.
199
200 $HS^- + H^+ \rightarrow H_2S.$ (2)
201
202 $2H_2S + O_2 \rightarrow S_2\downarrow + 2H_2O$ (3)
203
204 Figure 2 shows the white precipitation under the scanning electron microscope (SEM) and its
205 element composition using energy dispersive spectroscopy. This finding confirmed the fact that
206 acid dilution resulted in white precipitation of sulfur. For this reason, the measured
207 concentrations of S using nitric acid dilution for alkali-activated slag paste were not correct and
208 thus not presented in this study.
209
210 **Figure 2** White precipitation and its element composition in diluted pore solution using nitric acid.
211
212 2.3 Thermodynamic analysis of pore solution
213
214 Thermodynamics is essential to the understanding of chemical reactions. Whether a solid can
215 potentially form or not can be predicted through the saturation index (SI) [17].
216
217 $SI = \log(IAP/K_{S0})$ (4)

where IAP and K_{S0} are the ion activity product and equilibrium solubility product of a solid respectively. A positive SI indicates oversaturation and thus the possibility that this solid phase can precipitate. If SI is negative, it means under-saturation and implies that this solid is unstable in equilibrium within such a solution. A SI of zero indicates equilibrium between solution and solid. However, SI can be misleading when comparing phases which dissociate into a different number of ions (N) [17]. For this reason, effective saturation index (ESI) is applied in this study for thermodynamic analysis of pore solution.

$$ESI = SI/N \quad (5)$$

Before performing the thermodynamic analysis of the pore solution, it is crucial to obtain the thermodynamic database. In AAMs, the thermodynamic database is only available for alkali-activated slag. For alkali-activated fly ash, the thermodynamic data have not been established yet. For this reason, the thermodynamic analysis was only performed for the pore solutions of the alkali-activated slag pastes. The Gibbs energy minimization software GEM-Selektor v.3 (http://gems.web.psi.ch/) [34, 35] and the thermodynamic database developed in [36, 37] for alkali-activated slag were used. The activities of ions were calculated using the measured elemental concentrations as the input.

2.4 Measurement of heat evolution rate

The heat evolution rate was measured using an isothermal calorimeter by following standard ASTM C1679 [38]. For the measurements of heat evolution at the elevated temperatures (40 °C

and 60 °C), internal mixing was used to avoid any temperature difference. Fly ash and alkaline activator were conditioned in the calorimeter at the measurement temperature. When the thermal equilibrium was reached, the alkaline activator was injected into the glass ampoule to be mixed with aluminosilicate precursor powder internally. Subsequently, the heat release rate was recorded.

2.5 X-ray diffraction (XRD) and Fourier transform infrared spectroscopy (FTIR)

XRD analysis was performed on the powdered samples using a Philips X'Pert diffractometer applying CuK_{α} radiation (λ = 1.54 Å). The samples were scanned between 5° and 70° 2-theta, with a step size of 0.02° 2-theta and a dwell time of 5 s per step. FTIR was performed using a Spectrum TM 100 Optical ATR-FTIR spectrometer over the wavelength range of 600 to 4000 cm^{-1} with a resolution of 4 cm^{-1}.

3 Results and discussion

3.1 Pore solution composition of alkali-activated slag paste

Figure 3 presents the concentrations of Si, Al, Ca, OH^-, K and Na (hereafter denoted as [Si], [Al], [Ca], [OH^-], [K] and [Na] respectively) in the pore solution of alkali-activated slag paste as a function of time up to 28 days. The pore solution data are listed in the Appendix. The pore solution composition was dominated by Na and OH^-, whereas much lower concentrations of Si, Al, K and Ca were observed. The most significant changes in the compositions of pore solutions in alkali-activated slag pastes took place during the first hours up to 3 days. This can be seen

from the changes of elemental concentrations with time, particularly the decreases of the [Si], [Na] and [OH^-]. The concentrations of Si, Al and Ca were in the order: [Si] > [Al] > [Ca]. The developments of the elemental concentrations with time will be further discussed in the section 3.5.

Figure 3 Elemental concentrations in the pore solutions of alkali-activated slag pastes. In the graphs, N and S indicate weight percentage of Na_2O and SiO_2 with respect to slag. The water to slag ratio was 0.4 and the curing temperature was 20 °C.

There was a strong decrease of [Si] during the initial period up to 3 days, and then the decrease of [Si] continued gradually with time for all samples. For sodium hydroxide activated slag system, the [Si] increased with the increase of Na_2O content. For sodium silicate activated system, the [Si] increased with the increase of Na_2O content after 1 day. The [Si] in the pore solution of sodium silicate activated slag paste was much higher than that in the sodium hydroxide activated slag paste with the same content of Na_2O. The higher [Si] for sodium silicate activated slag paste was a result of the soluble Si in the sodium silicate activator. For all the alkali-activated slag samples, the [Al] decreased slightly with time. The increase of Na_2O content in alkaline activator led to an obvious increase of the [Al].

The [OH^-] decreased over time and increased with the increase of Na_2O content. Comparing the sodium silicate activated sample to the sodium hydroxide activated sample with the same content of Na_2O, it can be seen that the added SiO_2 from alkaline activator resulted in a decrease of [OH^-]. The [OH^-] indicates a pH in the range of 13.77~14.67 up to 28 days in the pore solution. This shows a higher alkalinity than that in the pore solution (pH>12) buffered by $Ca(OH)_2$ in OPC-

based materials, and much higher than the pH of 9.5 below which corrosion commences [39]. The [Ca] remained at a very low level (0.2~2 mmol/L) and did not show much change over time.

An apparent decrease of [Na] was observed during the first 3 days in Figure 3(E). And then the [Na] decreased slightly with progressive reaction of slag. When the Na_2O content increased from 4% to 8%, the [Na] increased for both the sodium hydroxide activated slag system and the sodium silicate activated slag system. On the contrary to the [Na], the [K] increased with time. This was because K was sourced from slag and increased with the dissolution of slag, while Na was mainly sourced from the alkaline activator and decreased as it was taken up into the calcium aluminosilicate hydrates [33, 40, 41].

In the pore solution of alkali-activated slag, the concentrations of Mg and Fe were not presented since they were below the detection limit of ICP-OES. The detection limit of Mg and Fe are 0.0042 mmol/L and 0.0009 mmol/L respectively. The concentration of Mg below the detection limit was attributed to the formation of a hydrotalcite-like phase in alkali-activated slag as seen from the XRD patterns (see Figure 8). The formation of hydrotalcite led Mg within the pore solution into hydrotalcite, and thus resulted into low concentration of Mg. The concentration of Fe below the detection limit was because of the low content of Fe_2O_3 in slag (0.46%). On the contrary, the concentrations of Mg and Fe were obtained for the alkali-activated fly ash pastes, which will be presented in section 3.3. This was because of no Mg containing phase detected in alkali-activated fly ash (see Figure 11) and much higher content of Fe_2O_3 in fly ash (6.6%).

The plots of the concentrations of Na, Al and Ca as a function of the concentration of OH^- are shown in Figure 4(A). In pore solutions, the positive charge of Na is mostly balanced by the

negative hydroxide ion. Higher [Na] leads to higher [OH^-]. For this reason, the concentration of Na increased linearly with the increase of the concentration of OH^- and this relationship was independent of the type of alkaline activator. In pore solutions, the concentration of Ca remained at a very low level and slightly decreased as the concentration of OH^- increased. This could be attributed to the common ion effect [42, 43]. The pore solutions had high concentrations of Si, OH^- and Na^+. Those ions might combine with Ca to form solid reaction products (see Table 4) and thus lowered the Ca concentration in the pore solution. This point could be further supported by thermodynamic analysis of pore solution (see section 3.2). The ESI with respect to C-(N-)A-S-H and secondary reaction products were mostly larger than zero, which indicates oversaturation and likely precipitation of these solid phases in pore solution. Therefore, Ca stayed on a low concentration and the increase of [OH^-] led to a decrease of the [Ca] in the pore solution.

The [Al] increased with the increase of [OH^-] in the pore solution for both the sodium hydroxide activated slag system and the sodium silicate activated slag system, which is consistent with the finding in the literature [24]. However, this relationship only exists for the samples using the same type of alkaline activator. Using the alkaline activator with the same content of Na_2O, the sodium hydroxide activated slag paste (e.g. N4S0) had higher [OH^-] in the pore solution than that of the sodium silicate activated slag paste (e.g. N4S5.4). But the pore solution of sodium hydroxide activated slag paste (e.g. N4S0) had a lower [Al] than that of sodium silicate activated slag paste (e.g. N4S5.4). This was because of the different calcium aluminosilicate hydrates formed as a consequence of the different types of alkaline activators used in the alkali activation of slag. The calcium aluminosilicate hydrate formed in the sodium hydroxide activated slag paste had a higher structural order than that formed in the sodium silicate activated slag paste [25]. This is also found in this work by XRD analysis (see Figure 8). For sodium hydroxide activated

samples (for instance N4S0), the peak that corresponded to C-(N-)A-S-H, was sharper and had a higher intensity than that for sodium silicate activated slag samples (for instance N4S5.4). Furthermore, C-S-H(I) was detected in sodium hydroxide activated slag samples while it was not in sodium silicate activated slag samples. As such, the calcium aluminosilicate hydrate formed in sodium hydroxide activated slag had higher structural order and degree of crosslinking. The higher structural order and degree of crosslinking of calcium aluminosilicate hydrate stabilized its structure, which could lead to a lower solubility. The lower solubility of calcium aluminosilicate hydrate resulted in lower solubility of Al and thus lower [Al] in the pore solution of sodium hydroxide activated slag paste.

Figure 4 Concentrations of one element as a function of the concentration of another element in pore solution. (A): [Na], [Al] and [Ca] versus [OH^-]. (B): [Si] versus [OH^-]. (C) [Si] versus [Ca]. In the graphs, N and S indicate the weight percentage of Na_2O and SiO_2 with respect to slag. The curing temperature was 20 °C. The water to slag ratio was 0.4.

In alkaline solutions, the solubility of Si increases with the increase of the alkalinity of solution [11]. This is also observed in the pore solution of sodium hydroxide activated slag paste [24]. In this study, the relationship between the alkalinity of pore solution and the solubility of Si was more comprehensively studied for sodium hydroxide activated slag pastes and sodium silicate activated slag pastes. Figure 4(B) shows the plots between the concentration of Si and the concentration of OH^- in the pore solution. The [Si] increased with the increase of [OH^-] in the pore solution for each alkali-activated slag paste. The plots suggest the existence of two separate lines as shown in Figure 4(B). The line with a higher [Si] is associated with the sodium silicate activated slag pastes, while the line with a lower [Si] corresponds to the sodium hydroxide

activated slag pastes. From the sodium hydroxide activated slag system to the sodium silicate activated slag system, the concentration of Si moves up and backward as indicated by the arrows. This is because of the addition of SiO_2 from the sodium silicate activator. On one hand, the addition of SiO_2 resulted in higher [Si] in the pore solution and thus an up translation of the plot. On the other hand, the addition of SiO_2 resulted in lower alkalinity of pore solution, e.g. lower [OH^-], and thus a backward translation of the plot.

Figure 4(C) plots the concentration of Si as a function of the concentration of Ca. As marked with a dashed black line in the graph, a decreasing trend was generally observed between the concentrations of Si and Ca, which is in line with the literature [24, 44]. The fact that the concentration of Si decreased with the increasing concentration of Ca was attributed to the common ion effect. Excess of Ca within pore solution could combine Si into solid reaction products and thus result in a lower concentration of Si.

3.2 Thermodynamic analysis of the pore solution of alkali-activated slag paste

As it is directly encoded in GEM-Selektor, the extended Debye-Huckel equation is used to calculate the ion activity coefficients [34, 35]. The extended Debye-Huckel equation is accurate at moderate ionic strengths (up to ~1-2 molal) [45]. Figure 5 presents the ionic strengths in the pore solution of alkali-activated slag paste. The ionic strengths in the pore solutions of N4S0, N4S5.4 and N6S5.4 were within 1-2 molal. In the pore solutions of N6S0, N8S0 and N8S5.4, the ionic strengths were larger than 2 molal, beyond the valid range (~1-2 molal). However, use of an improved aqueous phases model, such as the Pitzer model [46], is limited in the current version of GEM-Selektor. This is because the description of aqueous silicate species in the database of

GEM-Selektor does not extend beyond dimeric silicate and aluminosilicate units [36]. On the other hand, GEM-Selektor has been commonly used in the thermodynamic modelling of the hydration of alkali-activated slag (with ionic strengths ~1-3 molal in the pore solution [12]), and the modelling results agreed well with the experimental data [37, 47, 48]. As such, slight excess of ionic strengths (> 2 molal) would not impose a serious impact on the calculation results. Since the measured elemental concentrations, including the concentration of OH^-, were used as input to calculate the activities of aqueous ions with GEM-Selektor, the calculated pH agreed with the measured one.

Figure 5 The ionic strengths in the pore solutions of alkali-activated slag pastes, calculated by GEM-Selektor. In the graphs, N and S indicate the weight percentage of Na_2O and SiO_2 with respect to slag. The curing temperature was 20 °C. The water to slag ratio was 0.4.

Myers et al. used a set of eight CNASH_ss end-members to describe the calcium aluminosilicate hydrates in alkali-activated slag [36]. These eight end-members and their corresponding dissociation reactions and equilibrium solubility products are presented in Table 4. Among the eight end-members for the calcium aluminosilicate hydrates, 5CA and INFCA are two C-A-S-H gel end-members, 5CNA and INFCNA are two C-N-A-S-H gel end-members, INFCN is a C-N-S-H gel end-member, and T2C*, T5C* and TobH* are three C-S-H gel end-members. The equilibrium solubility products of these eight end-members were used to calculate the effective saturation indexes as described in section 2.3.

Table 4 Chemical reactions and equilibrium solubility products at 25℃ and 1 bar for eight end-members and crystalline reaction products in alkali-activated slag

Figure 6 presents the effective saturation indexes with respect to the eight end-members. For the sodium hydroxide activated slag pastes (the left column in Figure 6), the pore solutions were oversaturated with respect to 5CA, 5CNA, INFCNA, INFCN, T2C* and T5C. The effective saturation indexes with respect to those end-member gels decreased with time during the initial period (up to 3 days). This indicates the continuous formation of the calcium aluminosilicate hydrates. The formation of the calcium aluminosilicate hydrates reduced the degree of oversaturation and thus led to decreases of the effective saturation indexes. After the initial period, the reaction of slag slowed down and stepped into a steady reaction stage controlled by diffusion processes [49]. In this reaction stage, there might exist a dynamic equilibrium between the dissolution of slag and the formation of the calcium aluminosilicate hydrates. For this reason, the effective saturation indexes with respect to 5CA, 5CNA, INFCNA, INFCN, T2C* and T5C showed no substantial change with time. Although the increase of Na_2O content resulted in higher alkalinity of the pore solution, it did not lead to significant influence on the effective saturation indexes with respect to the eight end-members.

For sodium silicate activated slag pastes (the right column in Figure 6), similar results were found. Compared to those for the sodium hydroxide activated slag pastes, the effective saturation indexes with respect to the eight end-members were slightly higher for the sodium silicate activated slag pastes. The slightly higher effective saturation indexes were attributed to the larger activity coefficients of SiO_3^{2-} and Ca^{2+} (two valence electrons) than those of Na^+ and OH^- (one valence electron). It can be seen in Figure 6 that the pore solution of sodium silicate activated slag paste had higher concentrations of Si, Al and Ca than that of sodium hydroxide activated

433 slag paste. As such, the pore solution of sodium silicate activated slag paste had higher effective
434 saturation indexes with respect to the eight end-members.

435

436 **Figure 6** Effective saturation indexes with respect to the eight end-members as functions of time. In the graphs, N
437 and S indicate the weight percentage of Na_2O and SiO_2 with respect to slag. The curing temperature was 20 °C. The
438 water to slag ratio was 0.4. A ESI of 0 indicates equilibrium between solution and solid; a positive ESI indicates
439 oversaturation and a negative ESI indicates undersaturation.

440

441 In addition to the calcium aluminosilicate hydrates, some crystalline reaction products are also
442 identified in alkali-activated slag, such as hydrotalcite [50], tetracalcium aluminate hydrate
443 (C_4AH_{13}) [50], katoite (C_3AH_6) [37] and stratlingite (C_2ASH_8) [51]. The dissociation reactions
444 and equilibrium solubility products of C_2ASH_8, C_3AH_6, C_4AH_{13} and portlandite ($Ca(OH)_2$) are
445 listed in Table 4. These products were also captured according to the effective saturation index
446 from thermodynamic calculations. Figure 7 plots the effective saturation indexes with respect to
447 C_2ASH_8, C_3AH_6, C_4AH_{13} and $Ca(OH)_2$ for the sodium hydroxide activated slag pastes (left
448 column) and the sodium silicate activated slag pastes (right column). Since the concentration of
449 Mg was not measured, the effective saturation index with respect to hydrotalcite was not
450 calculated. The effective saturation indexes with respect to C_2ASH_8, C_3AH_6, C_4AH_{13} and
451 $Ca(OH)_2$ increased rapidly during the initial period. This is in the contrast to the effective
452 saturation indexes with respect to 5CA, 5CNA, INFCNA, INFCN, T2C* and T5C. It indicates
453 that the calcium aluminosilicate hydrate is thermodynamically favored to form at early age, while
454 the crystalline reaction products are thermodynamically favored to form at a later age. After the
455 initial period, the effective saturation indexes with respect to these four crystalline phases showed
456 no substantial change with time. The effective saturation indexes with respect to these four

457 crystalline phases were in the order: ESI(C_2ASH_8) > ESI(C_3AH_6) > ESI($Ca(OH)_2$) ≥
458 ESI(C_4AH_{13}) for the sodium hydroxide activated slag pastes, and ESI(C_2ASH_8) > ESI(C_3AH_6) >
459 ESI(C_4AH_{13}) ≥ ESI($Ca(OH)_2$) for the sodium silicate activated slag pastes.

460

461 **Figure 7** Effective saturation indexes with respect to C_2ASH_8, C_3AH_6, C_4AH_{13} and $Ca(OH)_2$ as functions of time. In
462 the graphs, N and S indicate the weight percentage of Na_2O and SiO_2 with respect to slag. The curing temperature
463 was 20 °C. The water to slag ratio was 0.4. A ESI of 0 indicates equilibrium between solution and solid; a positive
464 ESI indicates oversaturation and a negative ESI indicates undersaturation.

465

466 In order to confirm the thermodynamic analysis results, solid phase analysis was conducted for
467 alkali-activated slag pastes using XRD. Figure 8 presents the XRD patterns of N4S0, N8S0 and
468 N4S5.4 at 28 days. It can be seen that hydrotalcite and katoite (C_3AH_6) were identified in all
469 samples, which is in line with previous studies [50, 52, 53]. As the Na_2O content increased from
470 4% to 8%, portlandite was detected. The diffusive peak at $2\theta = 29.07°$ was dominant in all alkali-
471 activated slag samples. This diffusive peak is associated with the calcium aluminosilicate
472 hydrates (C-(N-)A-S-H) [52, 54]. According to the previous studies [50, 52, 54], the peaks at
473 approximately $2\theta = 7.0°$, 32.0° and 49.8° are attributed to the poorly crystalline C-S-H(I). The
474 poorly crystalline C-S-H(I) is considered more ordered than the C-S-H in ordinary Portland
475 cement paste at ambient temperature [55] and has been observed in alkali-activated slag [56]. It is
476 noted that C-S-H(I) was only detected in sodium hydroxide activated slag samples. The XRD
477 results validated the thermodynamic analysis using effective saturation index. The solid reaction
478 products with positive effective saturation indexes were likely to precipitate, such as calcium
479 aluminosilicate hydrate, katoite and portlandite.

480

Figure 8 X-ray diffraction patterns of N4S0, N8S0 and N4S5.4 at 28 days. In the graphs, N and S indicate the weight percentage of Na_2O and SiO_2 with respect to slag. The curing temperature was 20 °C. The water to slag ratio was 0.4.

3.3 Pore solution composition of alkali-activated fly ash paste

Figure 9 presents the measured concentrations of Si, Al, OH^-, Ca, Na, K, Fe, Mg and S in the pore solution of alkali-activated fly ash pastes as a function of time up to 28 days (672 hours). The pore solution data are listed in the Appendix. The pore solution composition was dominated by Na, OH^- and Si, whereas much lower concentrations of Al, K, Ca, Fe and Mg were observed. The most significant changes in the compositions of pore solutions in alkali-activated fly ash pastes took place during the first week. This can be seen from the changes of elemental concentrations with time, particularly the decreases of the [Si], [Na] and [OH^-]. The concentrations of Si, Al and Ca were in the order: [Si] > [Al] > [Ca]. The developments of the elemental concentrations with time will be further discussed in the section 3.5. The increase of curing temperature from 40 °C to 60 °C led to decreases of the concentrations of Si, Al, OH^-, Ca, Na, K, Fe and Mg. The influence of temperature on the pore solution composition of alkali-activated fly ash paste will be discussed in the section 3.6.

Figure 9 Elemental concentrations in the pore solutions of alkali-activated fly ash pastes where N and S indicate the weight percentage of Na_2O and SiO_2 with respect to fly ash, and T indicates the curing temperature in Celsius. The water to fly ash ratio was 0.35.

It can been seen from Figure 9(A) that the [Si] decreased with time for all alkali-activated fly ash pastes. As the Na_2O content increased from 6.2% to 9.3%, the [Si] increased for both curing

temperatures. The [Si] was much higher in the sodium silicate activated fly ash paste than that in the sodium hydroxide activated fly ash paste with the same content of Na_2O. This was attributed to the soluble silica added from the alkaline activator prepared using sodium silicate solution.

As shown in Figure 9(B), the [Al] decreased with time for all alkali-activated fly ash samples. For the sodium hydroxide activated fly ash pastes, the [Al] increased slightly as the Na_2O content increased from 6.2% to 9.3%. When the sodium silicate was added in the alkaline activator, the [Al] increased significantly in comparison with the sodium hydroxide activated fly ash with the same content of Na_2O, e.g. N9.3S9T40 in comparison with N9.3S0T40, and N9.3S9T60 in comparison with N9.3S0T60. The significantly increased [Al] in the sodium silicate activated fly ash paste was due to the enhanced dissolution of fly ash by the soluble silicate.

In the sodium hydroxide activated fly ash paste, the initial preferential dissolution of Al from the fly ash created a siliceous layer on the fly ash grains [57-59]. The initially dissolved aqueous Al species then might absorb to the surface sites on the siliceous layer, passivating the surface by preventing the approach of hydroxide ions [60]. Thus, the dissolution of fly ash could be slowed down. In the sodium silicate activated fly ash paste, the soluble silicate could quickly complex the initial preferentially released Al. This prevented Al from absorbing to the surface sites and thus reduced the surface passivation and allowed more rapid dissolution of fly ash [61]. It was reported that the soluble silicate enhanced greater structural breakdown of the frameworks in fly ash if the concentration of Si in the alkaline activator was larger than 213.6 mmol/L [61]. In this study, the concentration of Si in the alkaline activator for the sodium silicate activated fly ash pastes (Table 3) was 4170 mmol/L, twenty times larger than 213.6 mmol/L. As a result, the dissolution of Si, Al, Ca, K, Fe and Mg from fly ash was enhanced.

The enhanced dissolution of fly ash by soluble silicate can be also supported by the calorimetry data. Figure 10 presents the heat evolution rates of sodium hydroxide activated fly ash and sodium silicate activated fly ash cured at 40 °C and 60 °C. Two calorimetric peaks could be identified on the heat evolution rate curves of sodium hydroxide activated fly ash samples cured at 40 °C and 60 °C. The first calorimetric peak (P_1) corresponds to the dissolution/wetting of fly ash, and the second calorimetric peak (P_2) corresponds to the acceleration of polymerization process of alkali-aluminosilicate type gel [62]. Compared to sodium hydroxide activated fly ash samples, only one peak was identified on the heat evolution rate curves of sodium silicate activated fly ash samples cured at 40 °C and 60 °C. The calorimetry data clearly illustrate the effect of soluble silicate on the dissolution of fly ash. In the sodium hydroxide activated fly ash, the absorbed Al passivated the surface of fly ash and slowed down the dissolution of fly ash. As a result, the acceleration of polymerization of alkali-aluminosilicate type gel was delayed and thus led to the occurrence of the second calorimetric peak. In the sodium silicate activated fly ash, the soluble silicate reduced the surface passivation and allowed rapid dissolution of fly ash. Consequently, the polymerization of alkali-aluminosilicate type gel was accelerated. As such, the calorimetric peak that corresponded to the polymerization was advanced and thus merged into the calorimetric peak that corresponded to the dissolution/wetting of fly ash. For this reason, the second calorimetric peak was not readily identified.

Figure 10 Heat evolution rates of sodium hydroxide activated fly ash and sodium silicate activated fly ash cured at 40 °C and 60 °C: (A) N9.3S0T40 in comparison with N9.3S9T40; and (B) N9.3S0T60 in comparison with N9.3S9T60. In the graphs, P_1 and P_2 refer to the first and second calorimetric peak respectively, N and S indicate the

weight percentage of Na_2O and SiO_2 with respect to fly ash, and T indicates the curing temperature in Celsius. The water to fly ash ratio was 0.35.

From Figure 9(C), it is clear that the [OH^-] decreased with time, and increased significantly with increase of Na_2O content for both curing temperatures. When sodium silicate was used as the alkaline activator, the [OH^-] decreased significantly in comparison with the sodium hydroxide activated fly ash with the same content of Na_2O. The decreased alkalinity caused by the increased modulus of alkaline activator (SiO_2/Na_2O) is in agreement with [63]. The [OH^-] indicates a pH range of 13.08~14.07 up to 28 days of curing. This pH range shows a higher alkalinity in the pore solution of alkali-activated fly ash than that in the pore solution (pH>12) buffered by $Ca(OH)_2$ in OPC based materials, and is much higher than the pH of 9.5 below which steel reinforcement corrosion commences [39].

The concentration of Ca is plotted in Figure 9(D). The pore solution of sodium silicate activated fly ash paste had higher [Ca] than that of sodium hydroxide activated fly ash paste with the same content of Na_2O. This can be attributed to the lower alkalinity of pore solution and the enhanced dissolution of fly ash by the soluble silicate. The [Ca] decreased with time, which is different from the [Ca] in the pore solutions of alkali-activated slag pastes where no substantial change of the [Ca] was observed. The decrease of [Ca] was due to the precipitation of Ca into solid reaction products, which was also observed in [61]. The precipitation of Ca into solid reaction products was further evidenced by the solid phase analysis through XRD. Figure 11 presents the XRD patterns of alkali-activated fly ash samples at 28 days. It can be seen that new crystalline phases were formed in addition to quartz (Q), mullite (M) and hematite (H). Chabazite (C) was formed in sodium hydroxide activated fly ash samples, while faujasite (F) was formed in sodium silicate

activated fly ash samples. Both of chabazite and faujasite contain Ca. In addition to the Ca containing crystalline phases, Ca might be also incorporated into N-A-S-H gels [64]. It has been reported that Na may be displaced by Ca through ion exchange on the surface of N-A-S-H, resulting in N-(C-)A-S-H gels [65].

Figure 11 X-ray diffraction patterns of alkali-activated fly ash samples cured at 40 °C and 60 °C: (A) N9.3S0T40 and N9.3S0T60; and (B) N9.3S9T40 and N9.3S9T60. In the graphs, Q, M, H, C, F and A refer to quartz, mullite, hematite, chabazite, faujasite and analcime respectively, N and S indicate the weight percentage of Na_2O and SiO_2 with respect to fly ash, and T indicates the curing temperature in Celsius. For all samples, the water to fly ash ratio was 0.35.

Figure 9(E) showed an apparent decrease of [Na] with time. When the Na_2O content increased from 6.2% to 9.3%, the [Na] increased in the sodium hydroxide activated fly ash system. From Figure 9(F), it is clear that the [K] decreased as a function of time for all samples, which is on the contrary to the [K] in the pore solutions of alkali-activated slag pastes (Figure 3(F)). In the sodium hydroxide/silicate activated fly ash based materials, sodium based crystalline phases are normally identified, such as Na-chabazite and hydroxysodalite [66, 67]. On the contrary, potassium based crystalline phases are rarely reported. This is due to the better zeolitization capabilities of sodium cations than those of potassium cations since the sodium cations are smaller than the potassium cations [68]. So, the decrease of [K] was most likely to be attributed to the formation of potassium-aluminosilicate (K-A-S-H) type gels. The formation of K-A-S-H in alkali-activated fly ash has been reported in the literature [69, 70]. The increase of Na_2O content from 6.2% to 9.3% did not show much influence on [K]. Comparing the sodium silicate activated fly ash paste to the sodium hydroxide activated fly ash paste with the same content of Na_2O, the

[K] increased about two times. This could be due to the enhanced dissolution of fly ash by the soluble silicate.

The concentrations of Fe and Mg in the pore solutions of alkali-activated fly ash pastes are plotted as a function of time in Figure 9(G) and Figure 9(H) respectively (hereafter denoted as [Fe] and [Mg] respectively). It is clear that the concentrations of Fe and Mg decreased with time. Since the dissolution of fly ash is enhanced in the sodium silicate activated fly ash paste, the concentrations of Fe and Mg were higher when compared to those in the sodium hydroxide activated fly ash paste with the same content of Na_2O.

Figure 9(I) plots the concentration of S as a function of time (hereafter denoted as [S]). The [S] increased with time for all alkali-activated fly ash samples. For sodium hydroxide activated fly ash, the [S] increased with increase of Na_2O content. Fly ash contains 0.73% of SO_3 (see Table 1). If the S in the fly ash is completely dissolved in the alkaline activator, the concentration of S is around 250 mmol/L. However, the [S] measured in the pore solution was around 350 mmol/L, much larger than 250 mmol/L. This was because of the decrease of the solution volume resulted from the dissolution/wetting of fly ash and the polymerization process of alkali-aluminosilicate type gel. It is known that the porosity of alkali-activated fly ash decreases with time [28]. This indicates the decrease of the volume of solution in the alkali-activated fly ash. Therefore, using the volume of alkaline activator to calculate the concentration of S would result in underestimation.

3.4 Pore solution composition of alkali-activated slag blended with fly ash paste

To study the influence of the replacement of slag by fly ash on the pore solution composition, one mixture of alkali-activated slag blended with fly ash was used in this study. Figure 12(A) presents the elemental concentrations in the pore solution of alkali-activated slag blended with fly ash (N6S5.4B). The pore solution data are listed in the Appendix. It can be seen that [Si], [Na] and [OH^-] decreased as a function of time, while [Al] and [Ca] did not show much change with time. The [OH^-] indicates a pH range of 14.05~14.37 up to 28 days. Compared to the alkali-activated slag (N6S5.4) with the same contents of Na_2O and SiO_2 as shown in Figure 12(B), 50 wt.% replacement of slag by fly ash did not result in a substantial change on the pore solution composition of alkali-activated slag blended with fly ash paste.

Figure 12 Elemental concentrations in the pore solutions of alkali-activated slag blended with fly ash paste (A), and alkali-activated slag paste (B). In the graphs, N and S indicate the weight percentage of Na_2O and SiO_2 with respect to the precursor (slag, or blend of slag and fly ash), and B indicates blend of slag and fly ash. The curing temperature was 20 °C. The water to precursor ratio was 0.4.

But at a later curing age, the pore solution of alkali-activated slag blended with fly ash paste had higher [Si] and lower [Na] than that of alkali-activated slag paste with the same alkaline activator. At 28 days (672 hours), the concentrations of Si and Na were 37.5 mmol/L and 1670.4 mmol/L respectively in the pore solution of alkali-activated slag blended with fly ash paste, while they were 11.9 mmol/L and 2517.7 mmol/L respectively in the pore solution of alkali-activated slag paste. The higher [Si] in the alkali-activated slag blended with fly ash paste was because fly ash contains more reactive SiO_2 (37%) than slag (32.9%). The lower [Na] in the alkali-activated slag blended with fly ash paste was because the replacement of slag by fly ash led to the formation of alkali-aluminosilicate type gel. The alkali-aluminosilicate type gel was reported to

be formed together with calcium aluminosilicate type gel in alkali-activated blend of slag and fly ash in the literature [64, 71, 72]. The co-existence of calcium-aluminosilicate and alkali-aluminosilicate type gels was also confirmed by the solid phase analysis through XRD and FTIR.

Figure 13(A) presents the XRD patterns of alkali-activated slag blended with fly ash and alkali-activated slag with the same alkaline activator, e.g. N6S5.4B in comparison with N6S5.4 at 28 days. Like in alkali-activated slag paste (N6S5.4), calcium aluminosilicate hydrate was also formed in alkali-activated slag blended with fly ash paste. Since alkali-aluminosilicate type gel is amorphous to semi-crystalline [73], it was not detected by XRD. As such, FTIR technique was used to investigate the bonding environments in non-crystalline phases. Figure 13(B) plots the FTIR spectra of N6S5.4B and N6S5.4 at 28 days. The overall broad band of interest was located between 800 and 1200 cm^{-1}. This band is associated with the asymmetric stretching mode of Si-O-T bonds (T: tetrahedral Si or Al), and is usually used to study the changes of the amorphous gel structure [74, 75]. The Si-O-T band was centered at 948 cm^{-1} in alkali-activated slag paste, while it was centered at 952 cm^{-1} in alkali-activated slag blended with fly ash paste. The shift of Si-O-T band towards to a higher wavenumber was attributed to the incorporation of fly ash that resulted in the formation of more crosslinked alkali-aluminosilicate type gel [64]. As such, it can be concluded that calcium aluminosilicate and alkali-aluminosilicate type gels were both formed in alkali-activated slag blended with fly ash paste (N6S5.4B).

Figure 13 Solid phase analysis of alkali-activated slag blended with fly ash and alkali-activated slag with the same alkaline activator: (A) X-ray patterns, and (B) FTIR spectra. In the graphs, Q, M, H, Ht, K and C-(N-)A-S-H refer to quartz, mullite, hematite, hydrotalcite, katoite and calcium aluminosilicate hydrate respectively, N and S indicate the

671 weight percentage of Na_2O and SiO_2 with respect to the precursor (slag, or blend of slag and fly ash), and B indicates
672 blend of slag and fly ash. The curing temperature was 20 °C. The water to precursor ratio was 0.4.
673
674 Compared to the calcium aluminosilicate hydrate type gel, the alkali-aluminosilicate type gel
675 takes up a larger amount of Na to balance the charge of Al in the bonding network [76]. As such,
676 the pore solution of alkali-activated slag blended with fly ash paste had a relatively lower
677 concentration of Na than that of alkali-activated slag paste with the same alkaline activator. The
678 leaching of Na from AAMs is driven by the concentration gradients between the pore solution
679 and the water that surrounds the materials [26]. From this point of view, the decreased
680 concentration of Na in the pore solution due to the replacement of slag by fly ash can lead to
681 decreases of the concentration gradients and thus reduce the leaching of Na in the alkali-activated
682 slag blended with fly ash paste.
683
684 3.5 Conceptual models to describe the elemental concentrations in the pore solutions of alkali-
685 activated slag/fly ash pastes
686
687 Figure 14(A) presents the conceptual model to describe the concentrations of Al, Ca, K, Fe, and
688 Mg. Since Al, Ca, K, Fe and Mg are sourced from the precursor, the concentrations of these
689 elements in the pore solution initially start from zero and increase with the progressive
690 dissolution of the precursor. When the concentrations of these elements increase to be
691 oversaturated with respect to solids, these elements are thermodynamically favored to precipitate
692 and form the solids. If there are nuclei of the solids formed and the nuclei reach a critical size, the
693 solids start to grow. The formation of nuclei and the growth of the solids consume the elements
694 that constitute the solids. In the meantime, the dissolution of the precursor continues, releasing

these elements into the pore solution. When the consumption rates of these elements exceed the release rates of these elements, the concentrations of these elements decrease with time. Since the continuous release of these elements can partially compensate the consumption of these elements, the concentrations of these elements keep oversaturated with respect to the solids with time. But the degrees of oversaturation with respect to the solids decrease because the consumption of these elements cannot be completely replenished by the dissolution of the precursor.

Since Si can be sourced from both the alkaline activator and the dissolution of the precursor, the conceptual model to describe the concentration of Si in the pore solution depends on the concentration of Si in the alkaline activator ($[Si]_0$). If $[Si]_0=0$ (Figure 14(B)), Si can only be sourced from the dissolution of the precursor and its concentration in the pore solution initially starts from zero and increase with the progressive dissolution of the precursor. When the release rate of Si is equal to the consumption rate of Si, the concentration of Si reaches the maximum concentration ($[Si]_{max}$), after which it decreases with time. If $0<[Si]_0<[Si]_{max}$ (Figure 14(C)), the concentration of Si in the pore solution initially starts from $[Si]_0$. Since $[Si]_0<[Si]_{max}$, the release rate of Si from the precursor is larger than the consumption rate of Si. So, the concentration of Si increases with the progressive dissolution of the precursor until it reaches $[Si]_{max}$, at this point the release rate of Si from fly ash is equal to the consumption rate of Si, after which it decreases with time. If $[Si]_0\geq [Si]_{max}$ (Figure 14(D)), the concentration of Si in the pore solution initially starts from $[Si]_0$ and decreases with time because the $[Si]_0$ enables a consumption rate that is not smaller than the release rate of Si.

Figure 14 Conceptual models to describe the concentrations of Al, Ca, K, Fe, Mg, Si, Na, OH^- and S in the pore solution of alkali-activated slag/fly ash paste. In the graphs, $[Si]_0$ is the concentration of Si in the alkaline activator. $[Si]_{max}$ is the maximum concentration of Si.

Figure 14(E) shows the conceptual model for the description of the concentrations of Na and OH^-. Besides trace amount of Na_2O in the precursors, Na in the pore solution is sourced from the alkaline activator. With the continuous formation of solids, for example the alkali-aluminosilicate type gel, the Na is consumed and thus the concentration of Na decreases with time. Although the dissolution of alkali-earth metals (Ca, Mg etc.) from the precursor may result in formation of hydroxyl ion in the pore solution, this amount of hydroxyl ions are much smaller than the amount consumed by the dissolution of Si and Al. So, the concentration of OH^- decreases with time. S is sourced from slag/fly ash. Since no S related solids precipitate (as no S containing phases identified, see Figures 8, 11 and 13(A)), the concentration of S in the pore solution increases with time and reaches a maximum when S is completely dissolved from the precursor (Figure 14(F)).

3.6 The influence of temperature on the pore solution composition of alkali-activated fly ash paste

The increase of temperature led to decreases of the elemental concentrations in the pore solutions of alkali-activated fly ash pastes (see Figure 9). The influence of temperature on the pore solution composition of alkali-activated fly ash pastes can be discussed from the aspects of kinetics and thermodynamics.

3.6.1 Kinetics

741

742 The dissolution of fly ash releases the elements into the pore solution, while the formation of
743 solid reaction products consumes the elements that constitute the solid reaction products. So, the
744 elemental concentrations in the pore solution depend on the competition between the dissolution
745 of fly ash and the formation of solid reaction products. The increase of temperature leads to
746 accelerations of both the dissolution of fly ash and the formation of solid reaction products [77,
747 78]. It means the increase of temperature accelerates both the release of elements from fly ash
748 and the consumption of these elements by the formation of solid reaction products.

749

750 Figure 15 plots the heat evolution rates of sodium hydroxide activated fly ash pastes at 40 °C and
751 60 °C. The calorimetric responses of sodium silicate activated fly ash pastes show only one
752 calorimetric peak (see Figure 10). This makes it impossible to separate the calorimetric response
753 that corresponds to the dissolution of fly ash, and the calorimetric response that corresponds to
754 the formation of alkali-aluminosilicate type gel. Thus, these results are not included in Figure 15.
755 Comparing the calorimetric responses at 60 °C to the calorimetric responses at 40 °C, it can be
756 seen that the increase of temperature led to a larger increase of the intensity of the second
757 calorimetric peak. This indicates the increase of temperature had a larger acceleration of the
758 formation of solid reaction products than that of the dissolution of fly ash.

759

760 **Figure 15** Heat evolution rates of alkali-activated fly ash pastes at 40 °C (A) and 60 °C (B). In the graphs, P_1 and P_2
761 refer to the first and second calorimetric peak respectively, N and S indicate the weight percentage of Na_2O and SiO_2
762 with respect to fly ash, and T indicates the curing temperature in Celsius. The water to fly ash ratio was 0.35.

763

Since the increase of temperature led to a larger acceleration of the consumption of elements than that of the release of elements, the consumption rates of elements exceed the release rates of elements at lower elemental concentrations. So, maximum elemental concentrations after the increase of temperature were smaller than the maximum concentrations before the increase of temperature. To show the influence of temperature on the pore solution composition of alkali-activated fly ash paste, Figure 16 plots the concentrations of Al, Ca, K, Fe and Mg before and after the increase of temperature. In the experiments, the alkali-activated fly ash pastes were in fluid state at the early curing time, which made it infeasible to collect the pore solution using the steel-die method. For this reason, the maximum elemental concentrations were not obtained. As shown in Figure 16, the experimental measurements started after the maximum elemental concentrations.

Figure 16 The influence of an increase of temperature on the concentrations of Al, Ca, K, Fe and Mg in the pore solution of alkali-activated fly ash paste. T_1 and T_2 are temperatures.

3.6.2 Thermodynamics

Thermodynamics assumes a solubility equilibrium between the solid and the aqueous species in the liquid that react to form the solid [17]. From this point of view, the solubility of the reaction products also influence the concentrations of the elements that react to form the solids. The alkali-aluminosilicate type gel, as the main solid reaction products in alkali-activated fly ash paste [79], is amorphous to semi-crystalline [73] and considered as the precursors to zeolites in the literature [75, 80]. It is reported that an increase of temperature leads to increase of long-range ordering and higher degree of crosslinking in alkali-aluminosilicate type gel [78, 81, 82].

This point can be further confirmed by the FTIR analysis. Figure 17 presents the infrared spectra of alkali-activated fly ash samples at 28 days. It can be observed that an increase of temperature (from 40 °C to 60 °C) led to the shift of the Si-O-T band to higher wavenumbers, from 971 to 980 cm^{-1} for sodium hydroxide activated fly ash and from 979 to 983 cm^{-1} for sodium silicate activated fly ash. The shift of Si-O-T band from a lower wavenumber to a higher wavenumber indicates a higher degree of crosslinking of alkali-aluminosilicate type gel [64] and that the structure of alkali-aluminosilicate type gel becomes more ordered and stable [75]. As such, an increase of temperature leads to a higher degree of crosslinking of alkali-aluminosilicate type gel and a more stable structure.

Figure 17 FTIR spectra of alkali-activated fly ash samples at 28 days. In the graph, N and S indicate the weight percentage of Na_2O and SiO_2 with respect to fly ash, and T indicates the curing temperature in Celsius. The water to fly ash ratio was 0.35.

The higher degree of crosslinking and more stable structure of alkali-aluminosilicate type gel could lead to a decrease of the solubility of alkali-aluminosilicate type gel. The decreased solubility of alkali-aluminosilicate type gel results in lower concentrations of the elements that react to form the alkali-aluminosilicate type gel. So, the increase of temperature from 40 °C to 60 °C led to decreases of the concentrations of Si, Al, Na and K that reacted to form alkali aluminosilicate type gel.

4 Conclusions

This study investigated the pore solution composition of alkali-activated slag/fly ash pastes by means of ICP-OES analysis technique. The following conclusions can be drawn based on this study:

(1) In preparation of the samples for the ICP-OES analysis, alkaline dilution should be used for determination of the concentration of S. The acid dilution results in evaporation of H_2S and white precipitation of S. In the pore solutions of alkali-activated slag/fly ash pastes, the elemental concentrations depend on the alkaline activator and curing temperature.

(2) The pore solutions of alkali-activated slag pastes are oversaturated with respect to solids. In the initial period, the effective saturation indexes with respect to calcium aluminosilicate hydrates are relatively high and decrease with time. On the contrary, the effective saturation indexes with respect to the crystalline phases increase rapidly. After the initial period, the effective saturation indexes show no substantial change with time.

(3) In the pore solutions of alkali-activated fly ash pastes, an increase of temperature leads to decreases of the concentrations of Si, Al, Ca, K, Fe and Mg, while the soluble silicate in the alkaline activator results in increases of these elemental concentrations.

(4) Compared to the alkali-activated slag paste with the same alkaline activator, 50 wt.% replacement of slag by fly ash does not result in a substantial influence on the pore solution composition of alkali-activated slag blended with fly ash paste.

(5) According to the experimental results, conceptual models are proposed to describe the elemental concentrations in the pore solutions. Based on the conceptual models, the influence of temperature on the pore solution composition of alkali-activated fly ash paste can be well interpreted. In addition, these conceptual models will help to develop kinetic models to describe quantitatively the developments of the elemental concentrations with time.

Acknowledgements

The China Scholarship Council (the Grant Number 201406160048) and Microlab in Delft University of Technology are greatly acknowledged. The help by Mr. Shizhe Zhang on FTIR test is appreciated. The authors also would like to extend their grateful thanks to the anonymous reviewers, whose comments helped to substantially improve the quality of this paper.

Appendix. Pore solution composition data of alkali-activated slag/fly ash pastes

The pore solution data, i.e. elemental concentrations of Si, Al, OH^-, Ca, Na, K, Fe, Mg and S, are listed in Tables A1-A9.

Table A1 Concentration of Si (mmol/L)

Table A2 Concentration of Al (mmol/L)

Table A3 Concentration of OH^- (mmol/L)

Table A4 Concentration of Ca (mmol/L)

Table A5 Concentration of Na (mmol/L)

Table A6 Concentration of K (mmol/L)

Table A7 Concentration of Fe (mmol/L)

Table A8 Concentration of Mg (mmol/L)

Table A9 Concentration of S (mmol/L)

References

[1] J.L. Provis, S.A. Bernal, Geopolymers and related alkali-activated materials, Annu. Rev. Mater. Res., 44 (2014) 299-327.

[2] J.L. Provis, Alkali-activated materials, Cem. Concr. Res., (2017).

[3] P. Duxson, J.L. Provis, G.C. Lukey, J.S. Van Deventer, The role of inorganic polymer technology in the development of 'green concrete', Cem. Concr. Res., 37 (2007) 1590-1597.

[4] J.S. van Deventer, J.L. Provis, P. Duxson, D.G. Brice, Chemical research and climate change as drivers in the commercial adoption of alkali activated materials, Waste and Biomass Valorization, 1 (2010) 145-155.

[5] J.S.J. van Deventer, J.L. Provis, P. Duxson, Technical and commercial progress in the adoption of geopolymer cement, Miner Eng, 29 (2012) 89-104.

[6] A. Fernández-Jiménez, J. Palomo, F. Puertas, Alkali-activated slag mortars: mechanical strength behaviour, Cem. Concr. Res., 29 (1999) 1313-1321.

[7] F. Pacheco-Torgal, Z. Abdollahnejad, A.F. Camões, M. Jamshidi, Y. Ding, Durability of alkali-activated binders: A clear advantage over Portland cement or an unproven issue?, Constr. Build. Mater., 30 (2012) 400-405.

[8] S.A. Bernal, J.L. Provis, Durability of Alkali- Activated Materials: Progress and Perspectives, J. Am. Ceram. Soc., 97 (2014) 997-1008.

[9] J. Miranda, A. Fernández-Jiménez, J. González, A. Palomo, Corrosion resistance in activated fly ash mortars, Cem. Concr. Res., 35 (2005) 1210-1217.

[10] C. Shi, Early hydration and microstructure development of alkali-activated slag cement pastes, Proceedings of the 10th International Congress on the Chemistry of Cement, Gothenburg, Sweden, 1997, pp. 3ii099.

[11] Z. Huanhai, W. Xuequan, X. Zhongzi, T. Mingshu, Kinetic study on hydration of alkali-activated slag, Cem. Concr. Res., 23 (1993) 1253-1258.

[12] A. Gruskovnjak, B. Lothenbach, L. Holzer, R. Figi, F. Winnefeld, Hydration of alkali-activated slag: comparison with ordinary Portland cement, Adv. Cem. Res., (2006) 119-128.

[13] M. Ben Haha, G. Le Saout, F. Winnefeld, B. Lothenbach, Influence of activator type on hydration kinetics, hydrate assemblage and microstructural development of alkali activated blast-furnace slags, Cem. Concr. Res., 41 (2011) 301-310.

[14] B.S. Gebregziabiher, R.J. Thomas, S. Peethamparan, Temperature and activator effect on early-age reaction kinetics of alkali-activated slag binders, Constr. Build. Mater., 113 (2016) 783-793.

[15] Y. Ma, J. Hu, G. Ye, The effect of activating solution on the mechanical strength, reaction rate, mineralogy, and microstructure of alkali-activated fly ash, J. Mater. Sci., 47 (2012) 4568-4578.

[16] D. Damidot, B. Lothenbach, D. Herfort, F.P. Glasser, Thermodynamics and cement science, Cem. Concr. Res., 41 (2011) 679-695.

[17] B. Lothenbach, Thermodynamic equilibrium calculations in cementitious systems, Mater. Struct., 43 (2010) 1413-1433.

[18] B. Lothenbach, D. Damidot, T. Matschei, J. Marchand, Thermodynamic modelling: State of knowledge and challenges, Adv. Cem. Res., 22 (2010) 211-223.

[19] V.O. Ozçelik, C.E. White, Nanoscale Charge-Balancing Mechanism in Alkali-Substituted Calcium–Silicate–Hydrate Gels, The journal of physical chemistry letters, 7 (2016) 5266-5272.

[20] M. Criado, A. Fernández-Jiménez, A.G. de la Torre, M.A.G. Aranda, A. Palomo, An XRD study of the effect of the SiO2/Na2O ratio on the alkali activation of fly ash, Cem. Concr. Res., 37 (2007) 671-679.

[21] D. Hobbs, Concrete deterioration: causes, diagnosis, and minimising risk, International Materials Reviews, 46 (2001) 117-144.

[22] S. Mundra, M. Criado, S.A. Bernal, J.L. Provis, Chloride-induced corrosion of steel rebars in simulated pore solutions of alkali-activated concretes, Cem. Concr. Res., 100 (2017) 385-397.

[23] S. Diamond, Particle morphologies in fly ash, Cem. Concr. Res., 16 (1986) 569-579.

[24] S. Song, H.M. Jennings, Pore solution chemistry of alkali-activated ground granulated blast-furnace slag1, Cem. Concr. Res., 29 (1999) 159-170.

[25] F. Puertas, A. Fernández-Jiménez, M.T. Blanco-Varela, Pore solution in alkali-activated slag cement pastes. Relation to the composition and structure of calcium silicate hydrate, Cem. Concr. Res., 34 (2004) 139-148.

[26] R.R. Lloyd, J.L. Provis, J.S. Van Deventer, Pore solution composition and alkali diffusion in inorganic polymer cement, Cem. Concr. Res., 40 (2010) 1386-1392.

[27] K. Scrivener, T. Füllmann, E. Gallucci, G. Walenta, E. Bermejo, Quantitative study of Portland cement hydration by X-ray diffraction/Rietveld analysis and independent methods, Cem. Concr. Res., 34 (2004) 1541-1547.

[28] Y. Ma, Microstructure and Engineering Properties of Alkali Activated Fly Ash -as an environment friendly alternative to Portland cement, Tu Delft, Delft University of Technology, 2013.

[29] W. Chen, H. Brouwers, The hydration of slag, part 1: reaction models for alkali-activated slag, J. Mater. Sci., 42 (2007) 428-443.

[30] A. Palomo, M.W. Grutzeck, M.T. Blanco, Alkali-activated fly ashes - A cement for the future, Cem. Concr. Res., 29 (1999) 1323-1329.

[31] X. Gao, Q. Yu, H. Brouwers, Reaction kinetics, gel character and strength of ambient temperature cured alkali activated slag–fly ash blends, Constr. Build. Mater., 80 (2015) 105-115.

[32] R.S. Barneyback Jr, S. Diamond, Expression and analysis of pore fluids from hardened cement pastes and mortars, Cem. Concr. Res., 11 (1981) 279-285.

[33] B. Lothenbach, A. Gruskovnjak, Hydration of alkali-activated slag: thermodynamic modelling, Adv. Cem. Res., 19 (2007) 81-92.

[34] D.A. Kulik, T. Wagner, S.V. Dmytrieva, G. Kosakowski, F.F. Hingerl, K.V. Chudnenko, U.R. Berner, GEM-Selektor geochemical modeling package: revised algorithm and GEMS3K numerical kernel for coupled simulation codes, Comput. Geosci., 17 (2013) 1-24.

[35] T. Wagner, D.A. Kulik, F.F. Hingerl, S.V. Dmytrieva, GEM-Selektor geochemical modeling package: TSolMod library and data interface for multicomponent phase models, Can. Mineral., 50 (2012) 1173-1195.

[36] R.J. Myers, S.A. Bernal, J.L. Provis, A thermodynamic model for C-(N-)A-S-H gel: CNASH-ss. Derivation and validation, Cem. Concr. Res., 66 (2014) 27-47.

[37] R.J. Myers, B. Lothenbach, S.A. Bernal, J.L. Provis, Thermodynamic modelling of alkali-activated slag cements, Appl. Geochem., 61 (2015) 233-247.

[38] A. C1679-14, Standard Practice for Measuring Hydration Kinetics of Hydraulic Cementitious Mixtures Using Isothermal Calorimetry, ASTM International, PA, West Conshohocken, 2014.

[39] S. Ahmad, Reinforcement corrosion in concrete structures, its monitoring and service life prediction—a review, Cem. Concr. Comp., 25 (2003) 459-471.

[40] S.-Y. Hong, F.P. Glasser, Alkali sorption by C-S-H and C-A-S-H gels: Part II. Role of alumina, Cem. Concr. Res., 32 (2002) 1101-1111.

[41] E. L'Hôpital, B. Lothenbach, K. Scrivener, D. Kulik, Alkali uptake in calcium alumina silicate hydrate (CASH), Cem. Concr. Res., 85 (2016) 122-136.

[42] C. Shi, R. Day, Selectivity of alkaline activators for the activation of slags, Cement, Concrete and Aggregates, 18 (1996) 8-14.

[43] D. Rothstein, J.J. Thomas, B.J. Christensen, H.M. Jennings, Solubility behavior of Ca-, S-, Al-, and Si-bearing solid phases in Portland cement pore solutions as a function of hydration time, Cem. Concr. Res., 32 (2002) 1663-1671.

[44] S. Song, D. Sohn, H. Jennings, T. Mason, Hydration of alkali-activated ground granulated blast furnace slag, J. Mater. Sci., 35 (2000) 249-257.

[45] H.C. Helgeson, D.H. Kirkham, G.C. Flowers, Theoretical prediction of the thermodynamic behavior of aqueous electrolytes by high pressures and temperatures; IV, Calculation of activity coefficients, osmotic coefficients, and apparent molal and standard and relative partial molal properties to 600 degrees C and 5kb, American journal of science, 281 (1981) 1249-1516.

[46] K.S. Pitzer, Ion interaction approach: theory and data correlation, Activity coefficients in electrolyte solutions, 1991, pp. 75-153.

[47] R.J. Myers, Thermodynamic Modelling of CaO-Al2O3-SiO2-H2O-Based Cements, University of Sheffield, Sheffield, 2015.

[48] R.J. Myers, S.A. Bernal, J.L. Provis, Phase diagrams for alkali-activated slag binders, Cem. Concr. Res., 95 (2017) 30-38.

[49] C.J. Shi, R.L. Day, A Calorimetric Study of Early Hydration of Alkali-Slag Cements, Cem. Concr. Res., 25 (1995) 1333-1346.

[50] S.-D. Wang, K.L. Scrivener, Hydration products of alkali activated slag cement, Cem. Concr. Res., 25 (1995) 561-571.

[51] I.G. Richardson, A.R. Brough, G.W. Groves, C.M. Dobson, The Characterization of Hardened Alkali-Activated Blast-Furnace Slag Pastes and the Nature of the Calcium Silicate Hydrate (C-S-H) Phase, Cem. Concr. Res., 24 (1994) 813-829.

[52] H. Ye, A. Radlińska, Quantitative Analysis of Phase Assemblage and Chemical Shrinkage of Alkali-Activated Slag, J. Adv. Concr. Technol., 14 (2016) 245-260.

[53] F. Bonk, J. Schneider, M.A. Cincotto, H. Panepucci, Characterization by multinuclear high-resolution NMR of hydration products in activated blast-furnace slag pastes, J. Am. Ceram. Soc., 86 (2003) 1712-1719.

[54] M.B. Haha, B. Lothenbach, G. Le Saout, F. Winnefeld, Influence of slag chemistry on the hydration of alkali-activated blast-furnace slag — Part I: Effect of MgO, Cem. Concr. Res., 41 (2011) 955-963.

[55] H.F. Taylor, Cement chemistry, Thomas Telford1997.

[56] J.E. Oh, P.J.M. Monteiro, S.S. Jun, S. Choi, S.M. Clark, The evolution of strength and crystalline phases for alkali-activated ground blast furnace slag and fly ash-based geopolymers, Cem. Concr. Res., 40 (2010) 189-196.

[57] J.-L. Devidal, J. Schott, J.-L. Dandurand, An experimental study of kaolinite dissolution and precipitation kinetics as a function of chemical affinity and solution composition at 150 C, 40 bars, and pH 2, 6.8, and 7.8, Geochim. Cosmochim. Acta, 61 (1997) 5165-5186.

[58] C.A. Rees, J.L. Provis, G.C. Lukey, J.S. van Deventer, The mechanism of geopolymer gel formation investigated through seeded nucleation, Colloids and Surfaces A: Physicochemical and Engineering Aspects, 318 (2008) 97-105.

[59] E.H. Oelkers, General kinetic description of multioxide silicate mineral and glass dissolution, Geochim. Cosmochim. Acta, 65 (2001) 3703-3719.

[60] R. Iler, Effect of adsorbed alumina on the solubility of amorphous silica in water, J. Colloid Interface Sci., 43 (1973) 399-408.

[61] W.K.W. Lee, J.S.J. van Deventer, Structural reorganisation of class F fly ash in alkaline silicate solutions, Colloid Surface A, 211 (2002) 49-66.

[62] S. Chithiraputhiran, N. Neithalath, Isothermal reaction kinetics and temperature dependence of alkali activation of slag, fly ash and their blends, Constr. Build. Mater., 45 (2013) 233-242.

[63] A. Fernández-Jiménez, F. Puertas, Effect of activator mix on the hydration and strength behaviour of alkali-activated slag cements, Adv. Cem. Res., 15 (2003) 129-136.

[64] I. Ismail, S.A. Bernal, J.L. Provis, R.S. Nicolas, S. Hamdan, J.S.J. van Deventer, Modification of phase evolution in alkali-activated blast furnace slag by the incorporation of fly ash, Cem. Concr. Comp., 45 (2014) 125-135.

[65] I. García-Lodeiro, A. Fernández-Jiménez, A. Palomo, D.E. Macphee, Effect of calcium additions on N–A–S–H cementitious gels, J. Am. Ceram. Soc., 93 (2010) 1934-1940.

[66] A. Fernandez-Jimenez, A. Palomo, I. Sobrados, J. Sanz, The role played by the reactive alumina content in the alkaline activation of fly ashes, Micropor Mesopor Mat, 91 (2006) 111-119.

[67] M. Criado, A. Fernández-Jiménez, A. Palomo, I. Sobrados, J. Sanz, Effect of the SiO2/Na2O ratio on the alkali activation of fly ash. Part II: 29Si MAS-NMR Survey, Micropor Mesopor Mat, 109 (2008) 525-534.

[68] A. Fernández-Jiménez, A. Palomo, M. Criado, Alkali activated fly ash binders. A comparative study between sodium and potassium activators, Mater Construcc, 56 (2006) 51-65.

[69] J. Davidovits, Geopolymers, Journal of thermal analysis, 37 (1991) 1633-1656.

[70] C.B. Cheah, W.K. Part, M. Ramli, The hybridizations of coal fly ash and wood ash for the fabrication of low alkalinity geopolymer load bearing block cured at ambient temperature, Constr. Build. Mater., 88 (2015) 41-55.

[71] S.A. Bernal, J.L. Provis, B. Walkley, R. San Nicolas, J.D. Gehman, D.G. Brice, A.R. Kilcullen, P. Duxson, J.S. van Deventer, Gel nanostructure in alkali-activated binders based on slag and fly ash, and effects of accelerated carbonation, Cem. Concr. Res., 53 (2013) 127-144.

[72] S. Puligilla, P. Mondal, Co-existence of aluminosilicate and calcium silicate gel characterized through selective dissolution and FTIR spectral subtraction, Cem. Concr. Res., 70 (2015) 39-49.

[73] J. Davidovits, Geopolymers: inorganic polymeric new materials, Journal of Thermal Analysis and calorimetry, 37 (1991) 1633-1656.

[74] C.A. Rees, J.L. Provis, G.C. Lukey, J.S. Van Deventer, In situ ATR-FTIR study of the early stages of fly ash geopolymer gel formation, Langmuir, 23 (2007) 9076-9082.

[75] M. Criado, A. Fernández-Jiménez, A. Palomo, Alkali activation of fly ash: Effect of the SiO2/Na2O ratio: Part I: FTIR study, Micropor Mesopor Mat, 106 (2007) 180-191.

[76] M.R. Rowles, B.H. O'Connor, Chemical and structural microanalysis of aluminosilicate geopolymers synthesized by sodium silicate activation of metakaolinite, J. Am. Ceram. Soc., 92 (2009) 2354-2361.

[77] D. Hardjito, B.V. Rangan, Development and properties of low-calcium fly ash-based geopolymer concrete, Curtin University of Technology, 2005.

[78] P. Duxson, A. Fernández-Jiménez, J. Provis, G. Lukey, A. Palomo, J. Van Deventer, Geopolymer technology: the current state of the art, J. Mater. Sci., 42 (2007) 2917-2933.

[79] A. Fernández-Jiménez, A. Palomo, Composition and microstructure of alkali activated fly ash binder: effect of the activator, Cem. Concr. Res., 35 (2005) 1984-1992.

[80] J.L. Provis, J.S.J. Van Deventer, Geopolymers: structures, processing, properties and industrial applications, Elsevier2009.

[81] R. Barrer, D. Mainwaring, Chemistry of soil minerals. Part XIII. Reactions of metakaolinite with single and mixed bases, Journal of the Chemical Society, Dalton Transactions, (1972) 2534-2546.

[82] C.E. White, J.L. Provis, T. Proffen, J.S. Van Deventer, The effects of temperature on the local structure of metakaolin-based geopolymer binder: A neutron pair distribution function investigation, J. Am. Ceram. Soc., 93 (2010) 3486-3492.

Tables

Table 1 Chemical compositions of blast furnace slag and fly ash (by weight, %)

Oxide	SiO_2	CaO	Al_2O_3	MgO	Fe_2O_3	SO_3	K_2O	TiO_2	L.I.*
Slag	32.91	40.96	11.85	9.23	0.46	1.61	0.33	1.00	1.15
Fly ash	52.90	4.36	26.96	1.50	6.60	0.73	1.31	1.14	3.37

*L.I. refers to loss on ignition.

Table 2 Mixture compositions and curing temperature

Sample[a]	Precursor	Na_2O[b]	SiO_2[b]	Curing temperature
N4S0	slag	4	0	20 °C
N6S0	slag	6	0	20 °C
N8S0	slag	8	0	20 °C
N4S2.7	slag	4	2.7	20 °C
N4S5.4	slag	4	5.4	20 °C
N6S5.4	slag	6	5.4	20 °C
N8S5.4	slag	8	5.4	20 °C
N6.2S0T40	fly ash	6.2	0	40 °C
N9.3S0T40	fly ash	9.3	0	40 °C
N9.3S9T40	fly ash	9.3	9	40 °C
N6.2S0T60	fly ash	6.2	0	60 °C
N9.3S0T60	fly ash	9.3	0	60 °C
N9.3S9T60	fly ash	9.3	9	60 °C
N6S5.4B	blend[c]	6	5.4	20 °C

[a]N and S indicates weight percentage of Na_2O and SiO_2 with respect to precursor, T indicates temperature in Celsius and B indicates blend of slag and fly ash.

[b]weight percentage with respect to precursor content (wt. %).

[c]blend = 50 wt. % slag + 50 wt. % fly ash.

Table 3 The pH and concentrations of Na, Si, and OH^- in the alkaline activators

Sample[a]	pH	[Na] (mmol/L)	[Si] (mmol/L)	[OH^-] (mmol/L)[b]
N4S0	14.31	3239	0	3239(1957)
N6S0	14.50	4857	0	4857(2517)
N8S0	14.64	6466	0	6466(2953)
N4S2.7	14.14	3204	1117	1757(831)
N4S5.4	13.87	3193	2227	821(261)
N6S5.4 and N6S5.4B	14.30	4773	2219	2218(578)
N8S5.4	14.52	6339	2211	3636(817)
N6.2S0T40 and N6.2S0T60	14.58	5731	0	5731(2766)
N9.3S0T40 and N9.3S0T60	14.79	8564	0	8564(3408)
N9.3S9T40 and N9.3S9T60	14.60	8340	4170	3908(257)

[a]N and S indicates weight percentage of Na_2O and SiO_2 with respect to precursor, T indicates temperature in Celsius and B indicates blend of slag and fly ash.

[b]The numbers outside the brackets were obtained by thermodynamic calculations including the hydroxide from NaOH(aq), while those inside the brackets were obtained by excluding the hydroxide from NaOH(aq).

Table 4 Chemical reactions and equilibrium solubility products at 25℃ and 1 bar for eight end-members and crystalline reaction products in alkali-activated slag

End-member	Chemical reactions	*Log K_{s0}*
C-(N-)A-S-H gel ideal solid solution eight end-members, 'CNASH_ss' model **[36]**		
5CA	$(CaO)_{1.25}\cdot(Al_2O_3)_{0.125}\cdot(SiO_2)\cdot(H_2O)_{1.625} \Leftrightarrow 1.25Ca^{2+} + SiO_3^{2-} + 0.25AlO_2^- + 0.25OH^- + 1.5H_2O$	-10.75
INFCA	$(CaO)\cdot(Al_2O_3)_{0.15625}\cdot(SiO_2)_{1.1875}\cdot(H_2O)_{1.65625} + 0.6875OH^- \Leftrightarrow Ca^{2+} + 1.1875SiO_3^{2-} + 0.3125AlO_2^- + 2H_2O$	-8.90
5CNA	$(CaO)_{1.25}\cdot(Na_2O)_{0.25}\cdot(Al_2O_3)_{0.125}\cdot(SiO_2)\cdot(H_2O)_{1.25} \Leftrightarrow 1.25Ca^{2+} + SiO_3^{2-} + 0.25AlO_2^- + 0.5Na^+ + 0.75OH^- + H_2O$	-10.40
INFCNA	$(CaO)\cdot(Na_2O)_{0.34375}\cdot(Al_2O_3)_{0.15625}\cdot(SiO_2)_{1.1875}\cdot(H_2O)_{1.3} \Leftrightarrow Ca^{2+} + 1.1875SiO_3^{2-} + 0.3125AlO_2^- + 0.6875Na^+ + 1.3125H_2O$	-10.00
INFCN	$(CaO)\cdot(Na_2O)_{0.3125}\cdot(SiO_2)_{1.5}\cdot(H_2O)_{1.1875} + 0.375OH^- \Leftrightarrow Ca^{2+} + 1.5SiO_3^{2-} + 0.625Na^+ + 1.375H_2O$	-10.70
T2C*	$(CaO)_{1.5}\cdot(SiO_2)\cdot(H_2O)_{2.5} \Leftrightarrow 1.5Ca^{2+} + SiO_3^{2-} + OH^- + 2H_2O$	-11.60
T5C*	$(CaO)_{1.25}\cdot(SiO_2)_{1.25}\cdot(H_2O)_{2.} \Leftrightarrow 1.25Ca^{2+} + 1.25SiO_3^{2-} + 2.5H_2O$	-10.50
TobH*	$(CaO)\cdot(SiO_2)_{1.5}\cdot(H_2O)_{2.5} + OH^- \Leftrightarrow Ca^{2+} + 1.5SiO_3^{2-} + 3H_2O$	-7.90
Crystalline reaction products in alkali-activated slag **[17, 33]**		
C_2ASH_8	$(CaO)_2\cdot(Al_2O_3)\cdot(SiO_2)\cdot(H_2O)_8 \Leftrightarrow 2Ca^{2+} + 2AlO_2^- + SiO_3^{2-} + 8H_2O$	-19.10
C_3AH_6	$(CaO)_3\cdot(Al_2O_3)\cdot(H_2O)_6 \Leftrightarrow 3Ca^{2+} + 2AlO_2^- + 4OH^- + 4H_2O$	-20.85
$Ca(OH)_2$	$Ca(OH)_2 \Leftrightarrow Ca^{2+} + 2OH^-$	-5.20
C_4AH_{13}	$(CaO)_4\cdot(Al_2O_3)\cdot(H_2O)_{13} \Leftrightarrow 4Ca^{2+} + 2AlO_2^- + 6OH^- + 10H_2O$	-25.41

Table A1 Concentration of Si (mmol/L)

Sample	Time (hours)						
	3	7	24	72	168	336	672
N4S0	24.9	17.9	9.6	5.9	4.6	4.5	3.7
N6S0	39.7	33.7	22.3	14.3	11.5	9.1	7.7
N8S0	44.6	45.7	42.2	27.4	21.4	18.4	16.3
N4S2.7	--[a]	--	13.6	7.6	6.1	5.5	5.1
N4S5.4	469.6	312.9	22.4	12.1	9.7	7.5	6.4
N6S5.4	172.6	40.9	29.0	18.4	15.6	13.6	11.9
N8S5.4	78.9	67.1	50.9	38.2	30.9	28.6	25.7
N6.2S0T40	--	--	--	990.9	922.5	--	219.1
N9.3S0T40	--	--	--	2123.4	1048.0	--	150.2
N9.3S9T40	--	--	--	1965.9	2089.6	--	1381.3
N6.2S0T60	--	--	1107.3	374.3	113.6	--	12.8
N9.3S0T60	--	--	1504.5	552.1	221.6	--	74
N9.3S9T60	--	--	2421.6	2043.6	1787.7	--	655.6
N6S5.4B	--	227.9	63.8	56.5	37.5	--	37.5

[a]-- means not measured.

Table A2 Concentration of Al (mmol/L)

Sample	Time (hours)						
	3	7	24	72	168	336	672
N4S0	10.3	10.2	9.7	8.8	8.4	7.9	7.5
N6S0	15.4	15.4	15.1	14.6	14.2	12.4	12.1
N8S0	24.4	23.3	22.9	21.6	20.4	19.5	19.1
N4S2.7	--[a]	--	15.7	15.4	14.4	14.4	13.3
N4S5.4	11.8	10.8	9.7	12.2	13.2	12.4	11.1
N6S5.4	17.3	23.3	22.3	22.1	21.7	20.6	18.9
N8S5.4	32.7	32.3	32.9	32.3	30.7	31.3	29.3
N6.2S0T40	--	--	--	41.7	22.7	--	2.0
N9.3S0T40	--	--	--	177.8	32.8	--	1.1
N9.3S9T40	--	--	--	207.9	144.0	--	12.8
N6.2S0T60	--	--	26.9	3.1	0.3	--	--
N9.3S0T60	--	--	35.8	4.4	1.0	--	0.3
N9.3S9T60	--	--	128.0	36.9	15.9	--	2.3
N6S5.4B	--	21.4	30.9	29.7	30.1	--	25.4

[a]-- means not measured.

Table A3 Concentration of OH^- (mmol/L)

Sample	Time (hours)						
	3	7	24	72	168	336	672
N4S0	2098	2153	1890	1667	1581	1410	1289
N6S0	2907	3145	2864	2640	2537	2468	2213
N8S0	4149	4076	3989	3910	3883	3572	3621
N4S2.7	--[a]	--	1372	1070	1100	1009	969
N4S5.4	--	--	833	783	803	702	589
N6S5.4	2251	2074	1882	1747	1550	1426	1270
N8S5.4	2926	2941	2695	2609	2478	2406	2163
N6.2S0T40	--	--	--	2525	1015	--	333
N9.3S0T40	--	--	--	--	2327	--	1177
N9.3S9T40	--	--	--	--	1292	--	424
N6.2S0T60	--	--	1223	432	218	--	119
N9.3S0T60	--	--	2295	1643	1290	--	628
N9.3S9T60	--	--	1486	610	250	--	202
N6S5.4B	--	2370	--	--	--	--	1128

[a]-- means not measured.

Table A4 Concentration of Ca (mmol/L)

Sample	Time (hours)						
	3	7	24	72	168	336	672
N4S0	0.64	0.58	0.63	0.66	0.67	0.81	0.76
N6S0	0.53	0.47	0.36	0.53	0.58	0.52	0.57
N8S0	0.59	0.56	0.51	0.44	0.59	0.56	0.54
N4S2.7	--[a]	--	0.32	0.32	0.34	0.35	0.39
N4S5.4	2.34	--	1.49	1.40	1.24	1.28	1.56
N6S5.4	0.58	0.46	0.51	0.49	0.60	0.65	0.75
N8S5.4	0.50	0.40	0.35	0.35	0.36	0.26	0.23
N6.2S0T40	--	--	--	4.05	2.83	--	1.52
N9.3S0T40	--	--	--	12.23	3.80	--	1.10
N9.3S9T40	--	--	--	17.23	16.1	--	1.67
N6.2S0T60	--	--	2.33	1.10	0.69	--	0.99
N9.3S0T60	--	--	2.70	0.98	0.61	--	0.71
N9.3S9T60	--	--	11.18	3.93	1.78	--	0.98
N6S5.4B	--	0.71	1.16	0.69	0.56	--	1.02

[a]-- means not measured.

Table A5 Concentration of Na (mmol/L)

Sample	Time (hours)						
	3	7	24	72	168	336	672
N4S0	2793	2729	2459	2184	2141	1948	1747
N6S0	4064	4231	3956	3606	3518	3467	3077
N8S0	6291	5542	5948	5722	5162	5374	5207
N4S2.7	--[a]	--	1994	1879	1862	1802	1735
N4S5.4	2436	2254	1426	1386	1508	1387	1343
N6S5.4	3252	3136	3007	2750	2664	2600	2518
N8S5.4	4370	4322	4160	4104	4149	4122	3774
N6.2S0T40	--	--	--	3990	2268	--	1323
N9.3S0T40	--	--	--	5287	3191	--	1680
N9.3S9T40	--	--	--	4450	3802	--	2155
N6.2S0T60	--	--	2489	1335	1027	--	792
N9.3S0T60	--	--	3117	2071	1651	--	1443
N9.3S9T60	--	--	3669	2612	2395	--	1631
N6S5.4B	--	3921	3189	2804	2515	--	1670

[a]-- means not measured.

Table A6 Concentration of K (mmol/L)

Sample	Time (hours)						
	3	7	24	72	168	336	672
N4S0	30.7	39.7	52.6	61.7	72.2	77.7	81.2
N6S0	40.6	53.6	65.4	83.0	98.6	109.8	124.5
N8S0	57.9	60.6	72.4	87.4	105.4	120.9	139.9
N4S2.7	--[a]	--	33.0	44.3	48.4	54.6	56.9
N4S5.4	7.6	8.5	15.7	26.0	33.6	32.8	35.4
N6S5.4	16.5	41.1	45.9	56.1	62.3	67.0	62.2
N8S5.4	52.0	56.7	68.1	78.3	88.5	94.9	93.2
N6.2S0T40	--	--	--	88.4	61.5	--	26.4
N9.3S0T40	--	--	--	81.9	49.0	--	24.9
N9.3S9T40	--	--	--	126.4	115.4	--	50.8
N6.2S0T60	--	--	56.6	22.5	14.8	--	9.8
N9.3S0T60	--	--	39.6	23.7	16.1	--	13.5
N9.3S9T60	--	--	104.0	59.5	49.9	--	24.4
N6S5.4B	--	20.0	37.2	46.4	50.7	--	44.1

[a]-- means not measured.

Table A7 Concentration of Fe (mmol/L)

Sample	Time (hours)			
	24	72	168	672
N6.2S0T40	--[a]	1.72	1.11	0.12
N9.3S0T40	--	9.05	1.49	--
N9.3S9T40	--	12.46	8.64	0.32
N6.2S0T60	0.88	0.15	--	--
N9.3S0T60	1.30	0.13	--	--
N9.3S9T60	4.375	1.55	0.52	0.20

[a]-- means not measured.

Table A8 Concentration of Mg (mmol/L)

Sample	Time (hours)			
	24	72	168	672
N6.2S0T40	--[a]	1.58	1.29	0.19
N9.3S0T40	--	8.04	1.19	0.09
N9.3S9T40	--	9.29	7.92	0.39
N6.2S0T60	0.75	0.13	--	--
N9.3S0T60	0.92	0.11	--	0.06
N9.3S9T60	3.83	1.21	1.42	0.18

[a]-- means not measured.

Table A9 Concentration of S (mmol/L)

Sample	Time (hours)			
	24	72	168	672
N6.2S0T40	--[a]	253	274	356
N9.3S0T40	--	345	367	449
N9.3S9T40	--	40	47	63
N6.2S0T60	238	287	339	317
N9.3S0T60	315	360	371	391
N9.3S9T60	20	25	25	40

[a]-- means not measured.

Figures

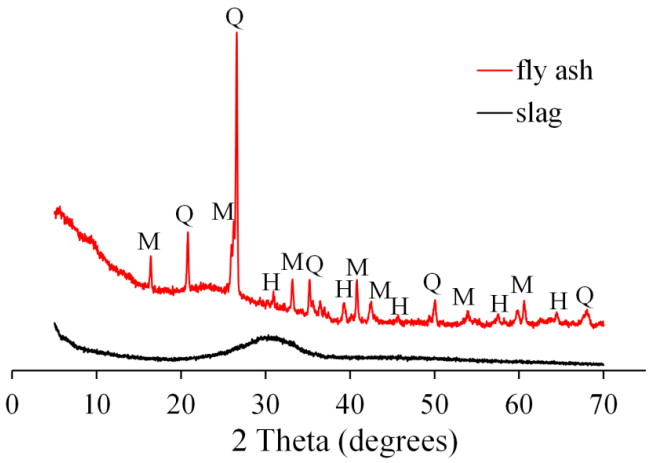

Figure 1 X-ray diffraction patterns of slag and fly ash. In the graph, Q, M and H refer to quartz, mullite and hematite respectively.

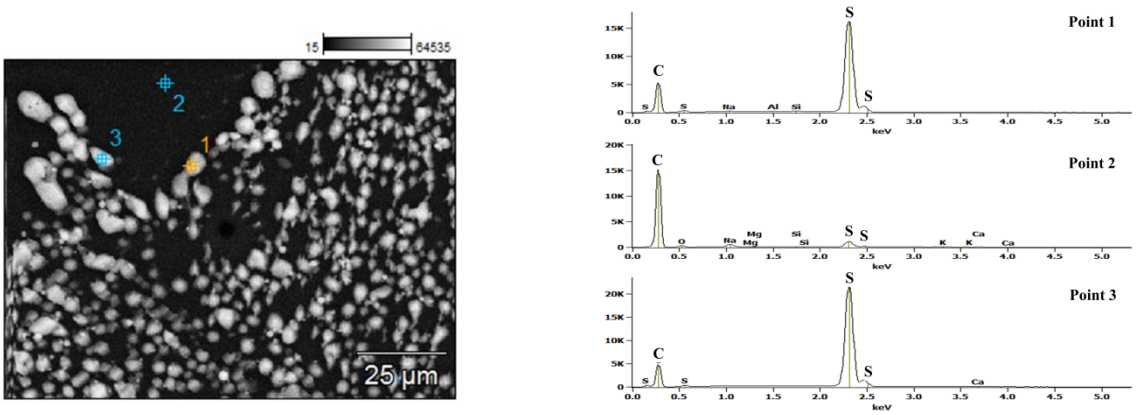

Figure 2 White precipitation and its element composition in diluted pore solution using nitric acid.

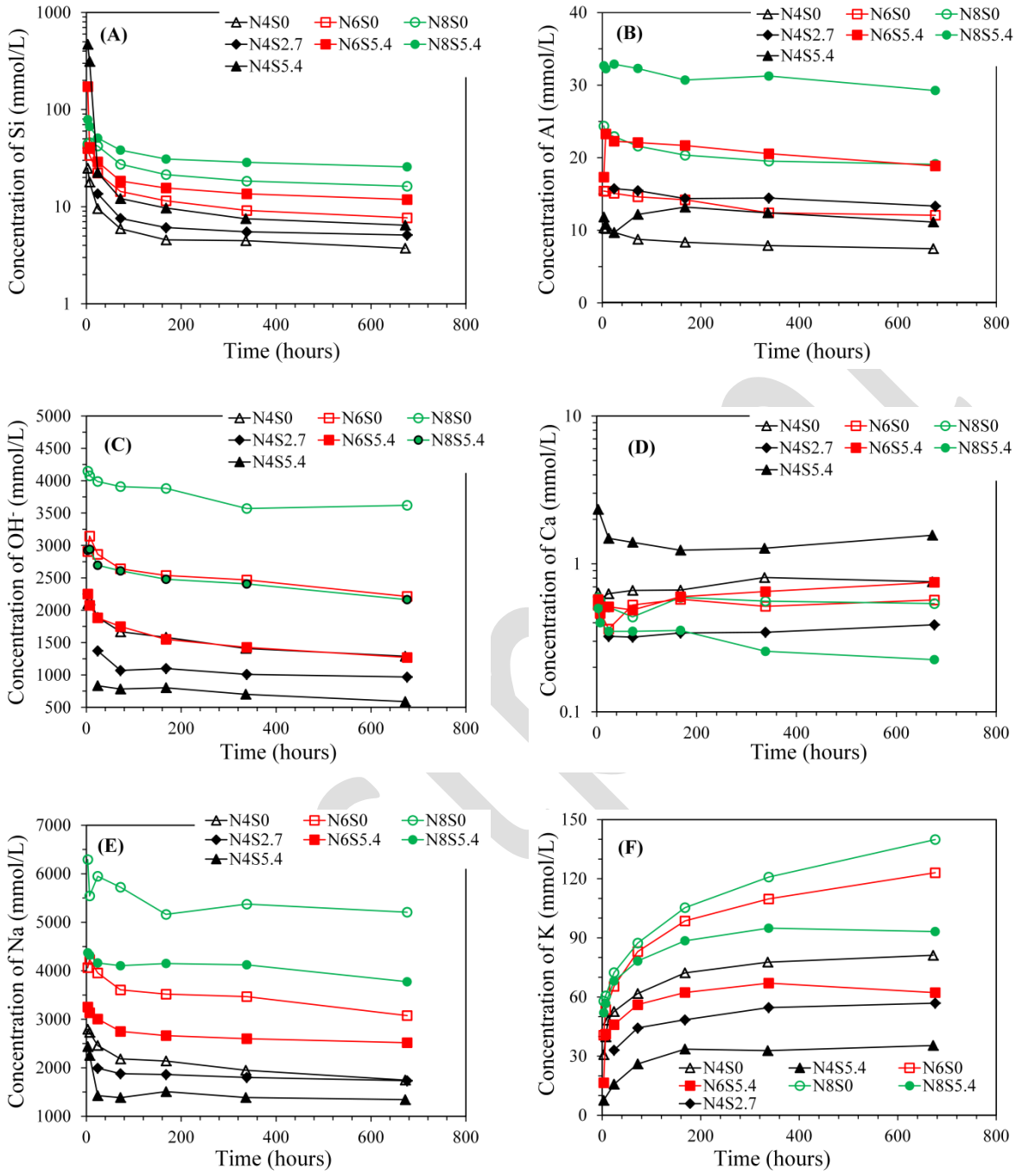

Figure 3 Elemental concentrations in the pore solutions of alkali-activated slag pastes. In the graphs, N and S indicate weight percentage of Na_2O and SiO_2 with respect to slag. The water to slag ratio was 0.4 and the curing temperature was 20 °C.

1223

1224

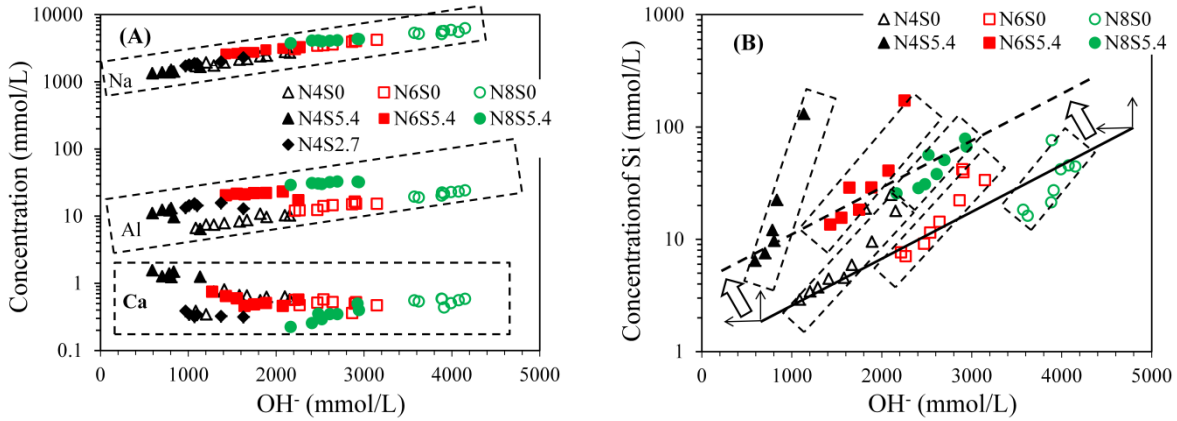

Figure 4 Concentrations of one element as a function of the concentration of another element in pore solution. (A): [Na], [Al] and [Ca] versus [OH^-]. (B): [Si] versus [OH^-]. (C) [Si] versus [Ca]. In the graphs, N and S indicate the weight percentage of Na_2O and SiO_2 with respect to slag. The curing temperature was 20 °C. The water to slag ratio was 0.4.

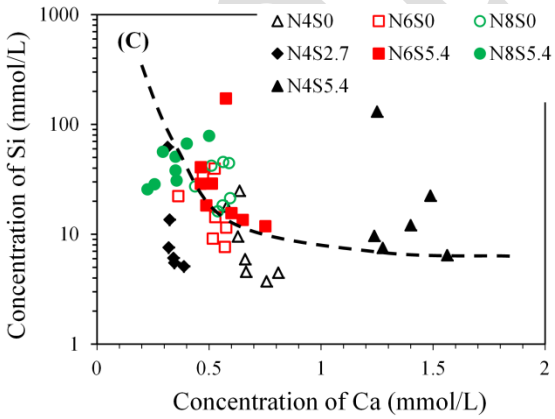

1225

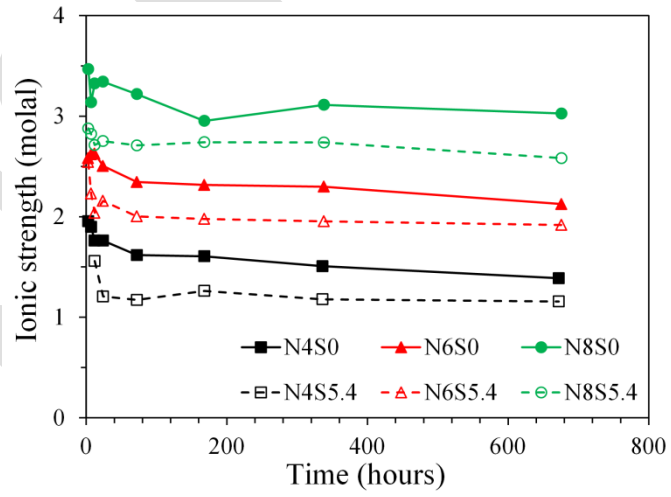

Figure 5 The ionic strengths in the pore solutions of alkali-activated slag pastes, calculated by GEM-Selektor. In the graphs, N and S indicate the weight percentage of Na_2O and SiO_2 with respect to slag. The curing temperature was 20 °C. The water to slag ratio was 0.4.

1226

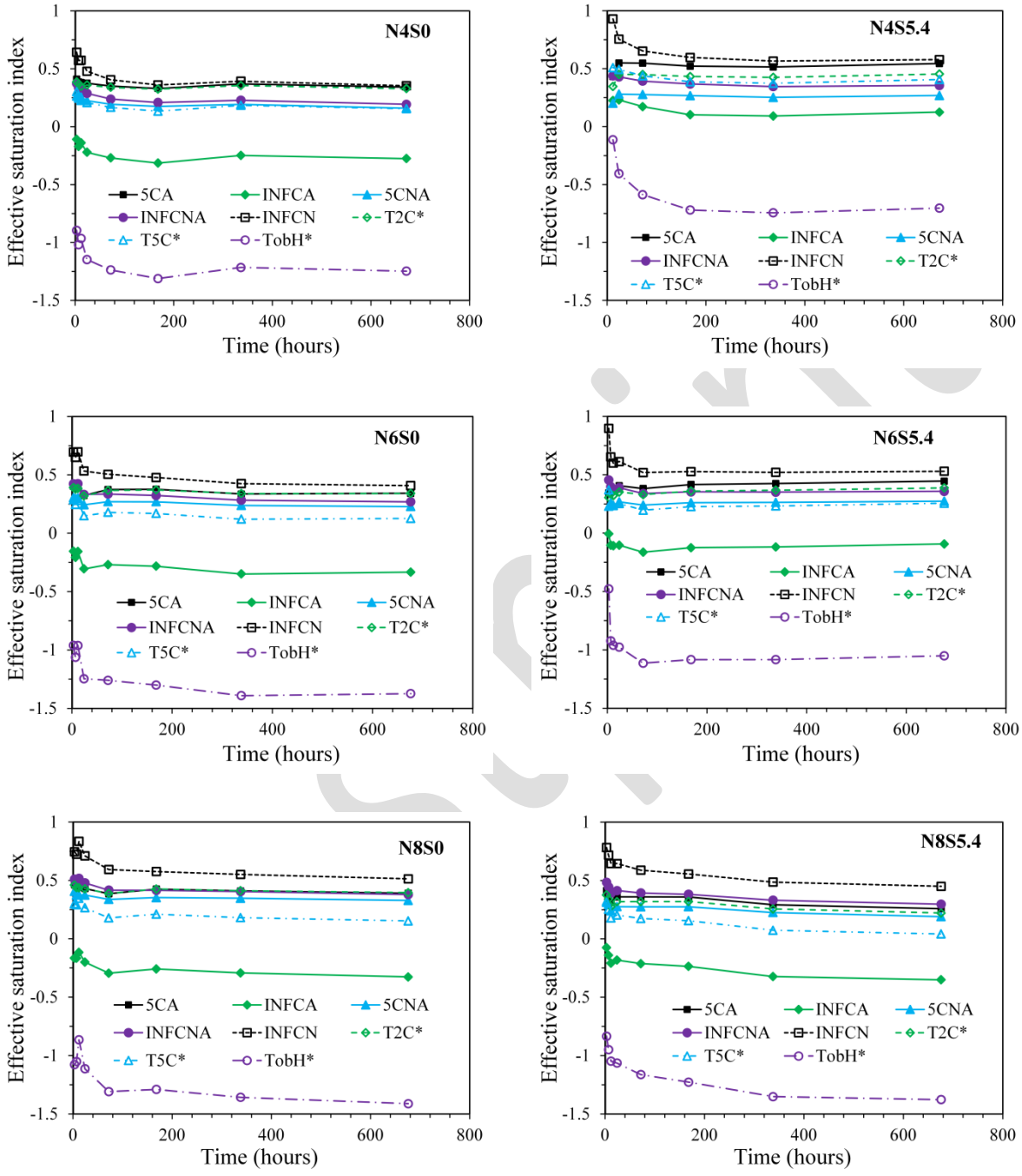

Figure 6 Effective saturation indexes with respect to the eight end-members as functions of time. In the graphs, N and S indicate the weight percentage of Na_2O and SiO_2 with respect to slag. The curing temperature was 20 °C. The water to slag ratio was 0.4. A ESI of 0 indicates equilibrium between solution and solid; a positive ESI indicates oversaturation and a negative ESI indicates undersaturation.

1227

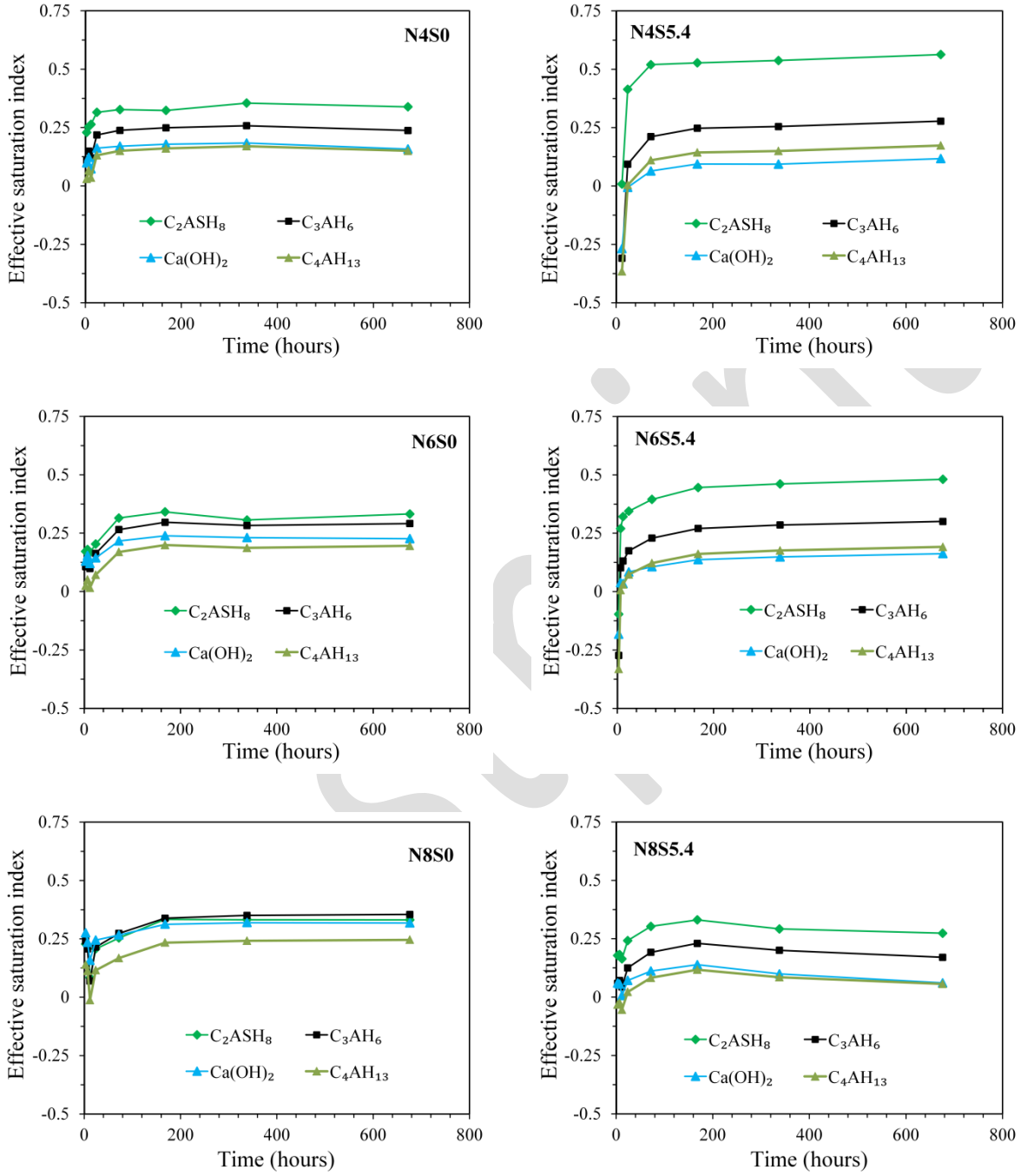

Figure 7 Effective saturation indexes with respect to C_2ASH_8, C_3AH_6, C_4AH_{13} and $Ca(OH)_2$ as functions of time. In the graphs, N and S indicate the weight percentage of Na_2O and SiO_2 with respect to slag. The curing temperature was 20 °C. The water to slag ratio was 0.4. A ESI of 0 indicates equilibrium between solution and solid; a positive ESI indicates oversaturation and a negative ESI indicates undersaturation.

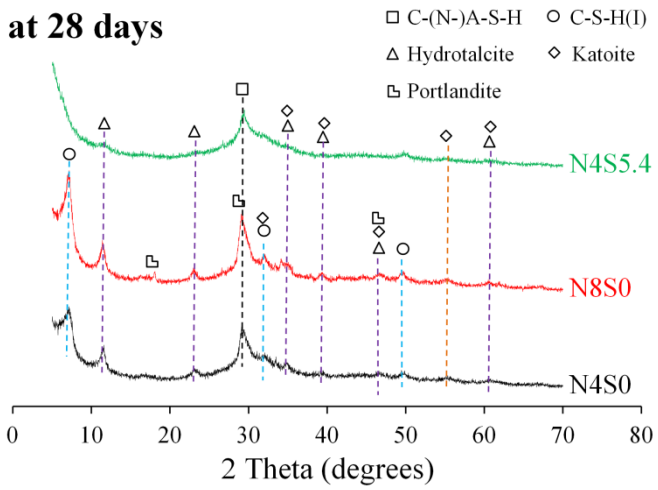

Figure 8 X-ray diffraction patterns of N4S0, N8S0 and N4S5.4 at 28 days. In the graphs, N and S indicate the weight percentage of Na_2O and SiO_2 with respect to slag. The curing temperature was 20 °C. The water to slag ratio was 0.4.

1228

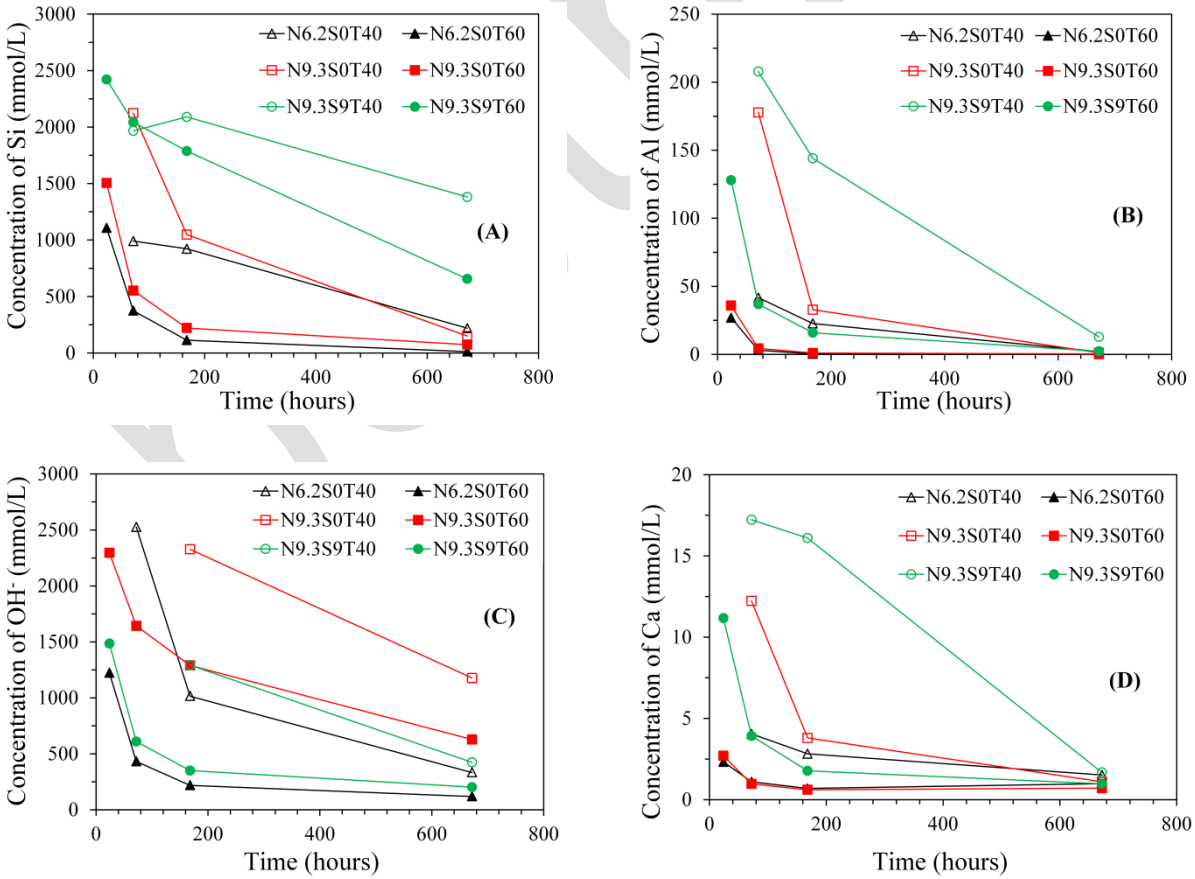

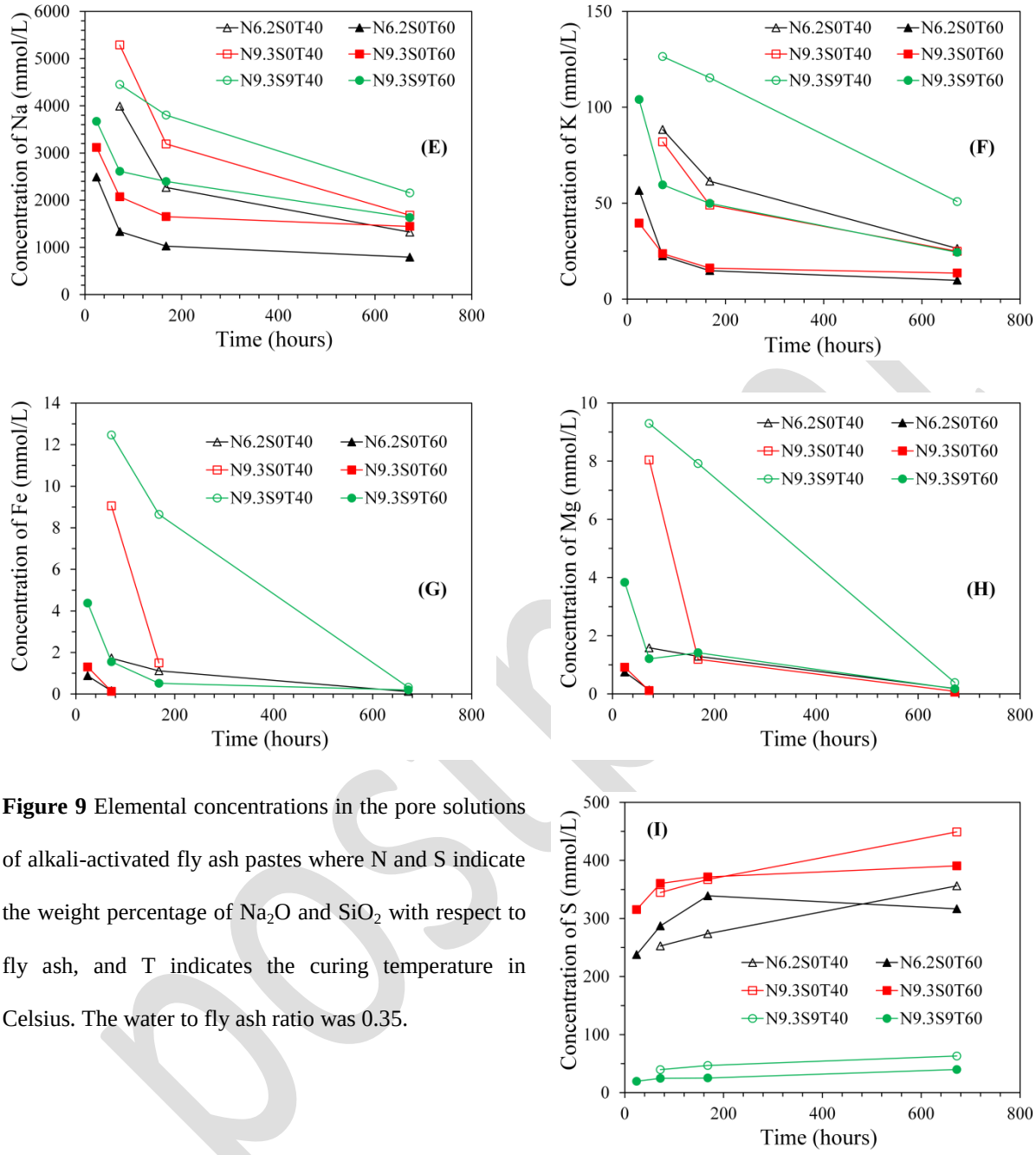

Figure 9 Elemental concentrations in the pore solutions of alkali-activated fly ash pastes where N and S indicate the weight percentage of Na_2O and SiO_2 with respect to fly ash, and T indicates the curing temperature in Celsius. The water to fly ash ratio was 0.35.

1229

1230

1231

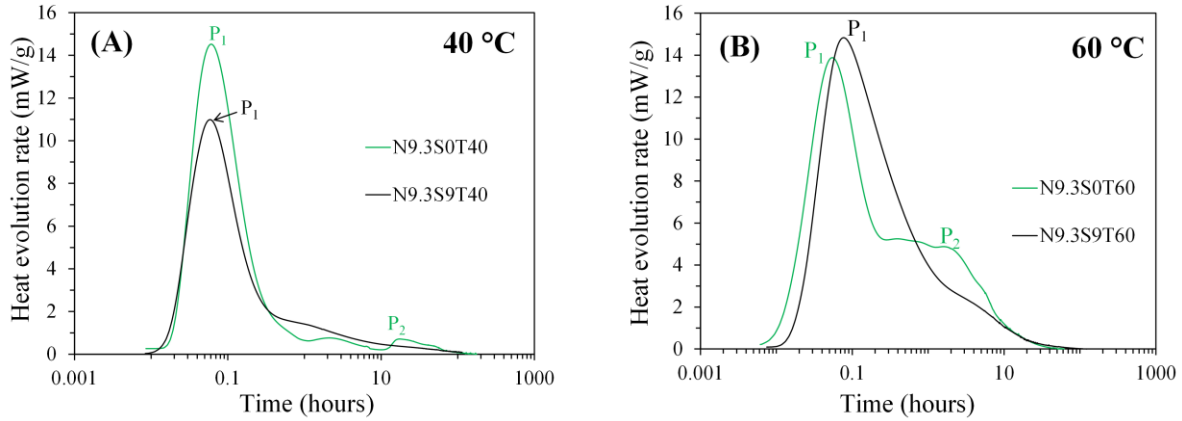

Figure 10 Heat evolution rates of sodium hydroxide activated fly ash and sodium silicate activated fly ash cured at 40 °C and 60 °C: (A) N9.3S0T40 in comparison with N9.3S9T40; and (B) N9.3S0T60 in comparison with N9.3S9T60. In the graphs, P_1 and P_2 refer to the first and second calorimetric peak respectively, N and S indicate the weight percentage of Na_2O and SiO_2 with respect to fly ash, and T indicates the curing temperature in Celsius. The water to fly ash ratio was 0.35.

1232

1233

1234

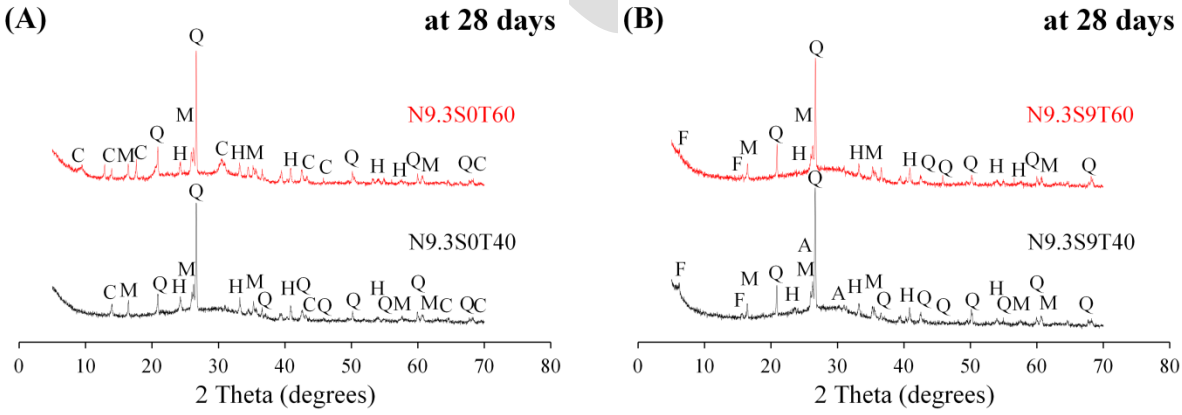

Figure 11 X-ray diffraction patterns of alkali-activated fly ash samples cured at 40 °C and 60 °C: (A) N9.3S0T40 and N9.3S0T60; and (B) N9.3S9T40 and N9.3S9T60. In the graphs, Q, M, H, C, F and A refer to quartz, mullite, hematite, chabazite, faujasite and analcime respectively, N and S indicate the weight percentage of Na_2O and SiO_2 with respect to fly ash, and T indicates the curing temperature in Celsius. For all samples, the water to fly ash ratio was 0.35.

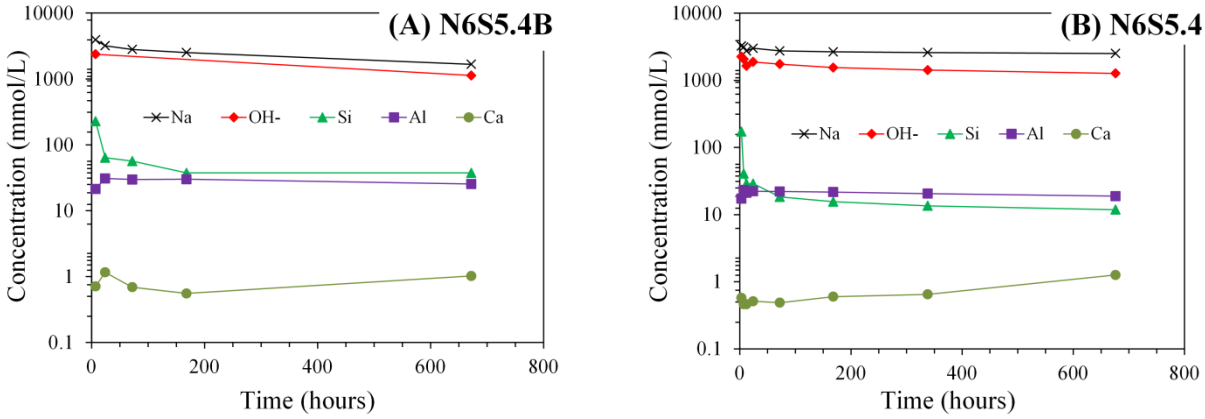

Figure 12 Elemental concentrations in the pore solutions of alkali-activated slag blended with fly ash paste (A), and alkali-activated slag paste (B). In the graphs, N and S indicate the weight percentage of Na_2O and SiO_2 with respect to the precursor (slag, or blend of slag and fly ash), and B indicates blend of slag and fly ash. The curing temperature was 20 °C. The water to precursor ratio was 0.4.

1235

1236

1237

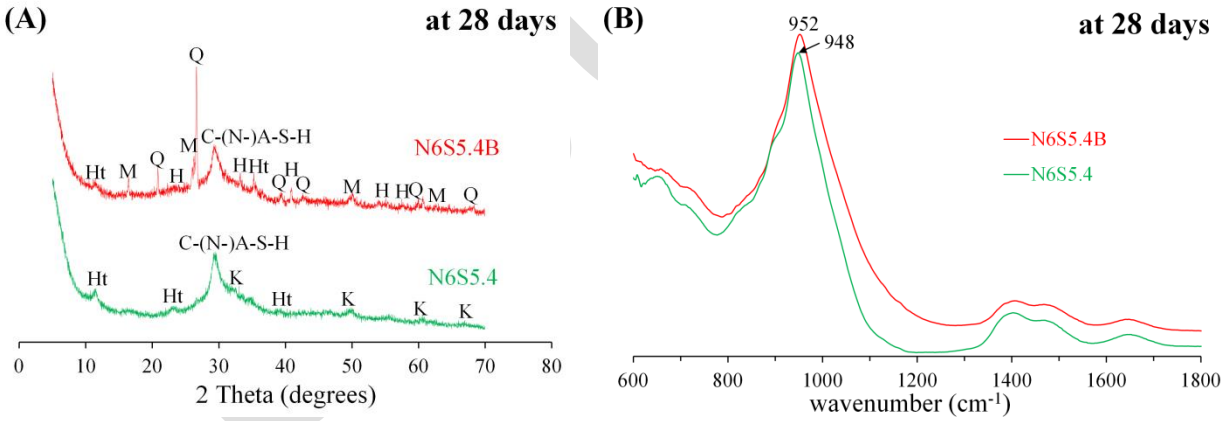

Figure 13 Solid phase analysis of alkali-activated slag blended with fly ash and alkali-activated slag with the same alkaline activator: (A) X-ray patterns, and (B) FTIR spectra. In the graphs, Q, M, H, Ht, K and C-(N-)A-S-H refer to quartz, mullite, hematite, hydrotalcite, katoite and calcium aluminosilicate hydrate respectively, N and S indicate the weight percentage of Na_2O and SiO_2 with respect to the precursor (slag, or blend of slag and fly ash), and B indicates blend of slag and fly ash. The curing temperature was 20 °C. The water to precursor ratio was 0.4.

1238

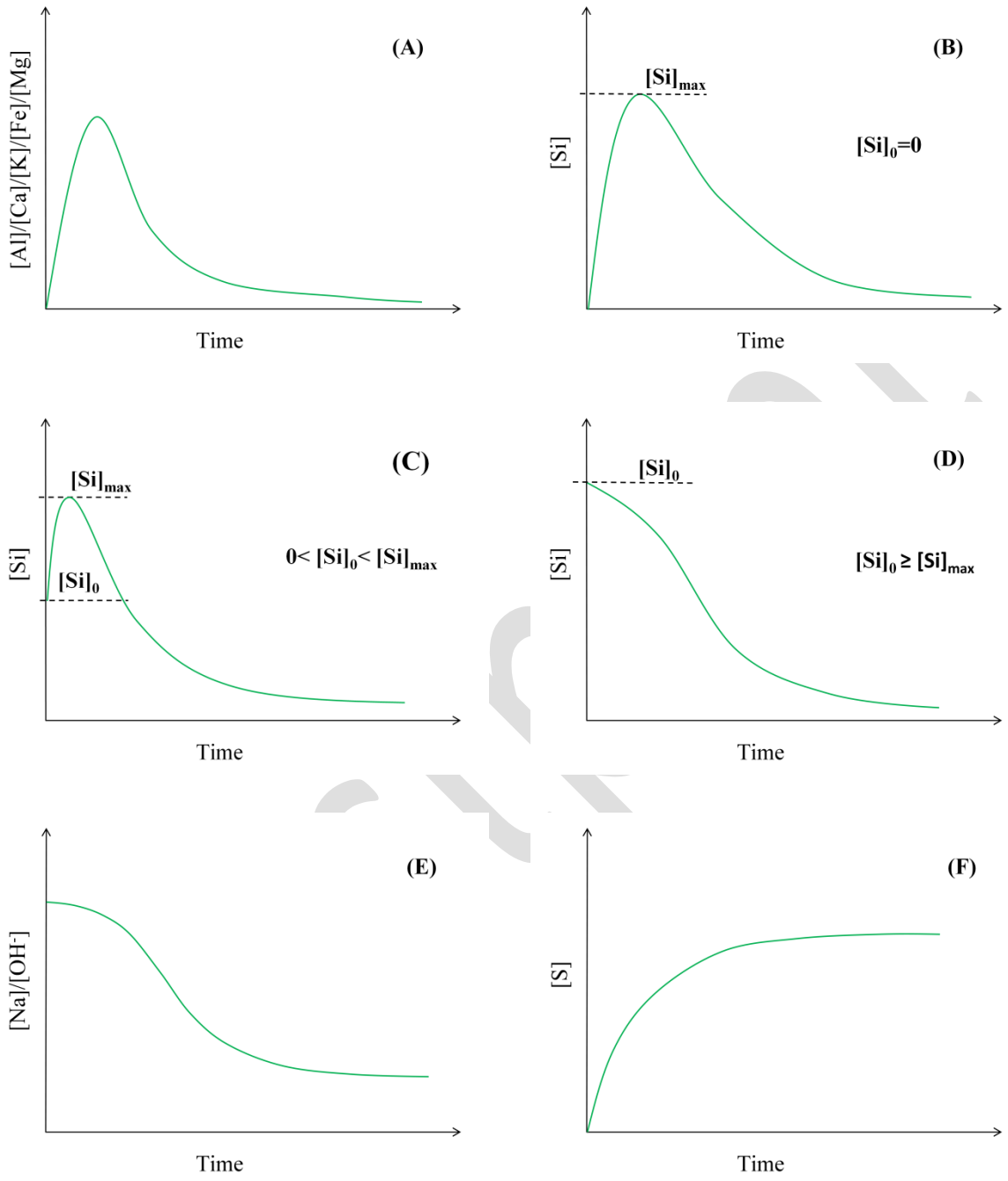

Figure 14 Conceptual models to describe the concentrations of Al, Ca, K, Fe, Mg, Si, Na, OH^- and S in the pore solution of alkali-activated slag/fly ash paste. In the graphs, $[Si]_0$ is the concentration of Si in the alkaline activator. $[Si]_{max}$ is the maximum concentration of Si.

1239

1240

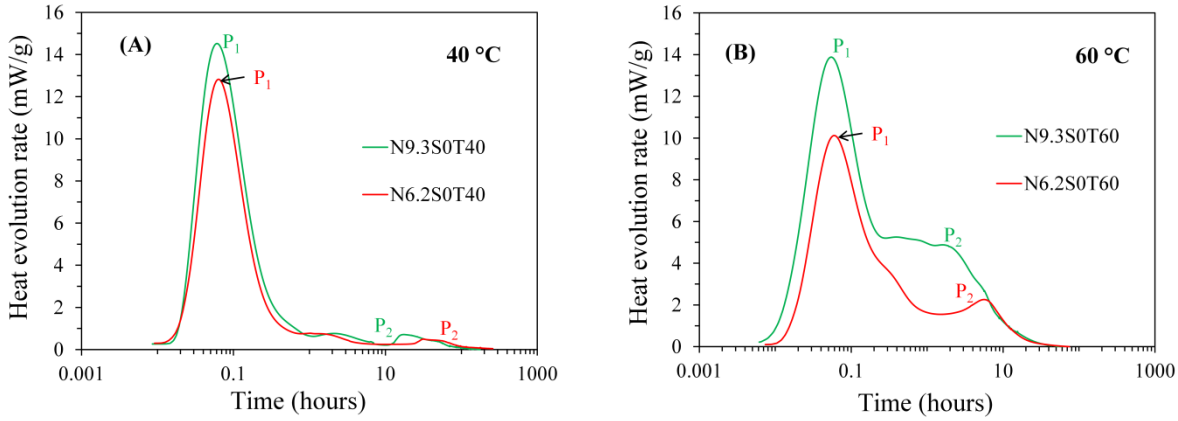

Figure 15 Heat evolution rates of alkali-activated fly ash pastes at 40 °C (A) and 60 °C (B). In the graphs, P_1 and P_2 refer to the first and second calorimetric peak respectively, N and S indicate the weight percentage of Na_2O and SiO_2 with respect to fly ash, and T indicates the curing temperature in Celsius. The water to fly ash ratio was 0.35.

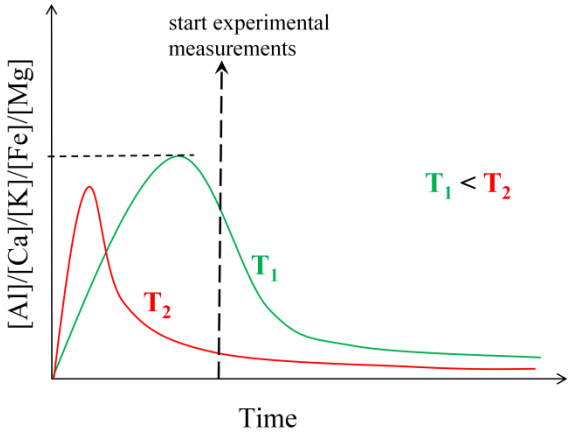

Figure 16 The influence of an increase of temperature on the concentrations of Al, Ca, K, Fe and Mg in the pore solution of alkali-activated fly ash paste. T_1 and T_2 are temperatures.

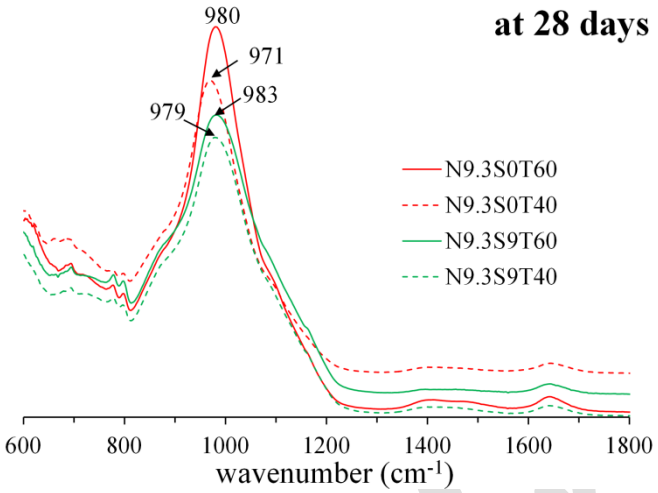

Figure 17 FTIR spectra of alkali-activated fly ash samples at 28 days. In the graph, N and S indicate the weight percentage of Na_2O and SiO_2 with respect to fly ash, and T indicates the curing temperature in Celsius. The water to fly ash ratio was 0.35.

1248